Opto-Electronic Science

ISSN 2097-0382 CN 51-1800/O4

A review of liquid crystal spatial light modulators: devices and applications

Yiqian Yang, Andrew Forbes and Liangcai Cao

Citation: Yang YQ, Forbes A, Cao LC. A review of liquid crystal spatial light modulators: devices and applications. *Opto-Electron Sci* **2**, 230026 (2023).

https://doi.org/10.29026/oes.2023.230026

Received: 10 August 2023; Accepted: 22 September 2023; Published online: 26 October 2023

Opto-Electronic Science

Review

August 2023, Vol. 2, No. 8

DOI: 10.29026/oes.2023.230026

A review of liquid crystal spatial light modulators: devices and applications

Yiqian Yang[1], Andrew Forbes[2]* and Liangcai Cao[1]*

Spatial light modulators, as dynamic flat-panel optical devices, have witnessed rapid development over the past two decades, concomitant with the advancements in micro- and opto-electronic integration technology. In particular, liquid-crystal spatial light modulator (LC-SLM) technologies have been regarded as versatile tools for generating arbitrary optical fields and tailoring all degrees of freedom beyond just phase and amplitude. These devices have gained significant interest in the nascent field of structured light in space and time, facilitated by their ease of use and real-time light manipulation, fueling both fundamental research and practical applications. Here we provide an overview of the key working principles of LC-SLMs and review the significant progress made to date in their deployment for various applications, covering topics as diverse as beam shaping and steering, holography, optical trapping and tweezers, measurement, wavefront coding, optical vortex, and quantum optics. Finally, we conclude with an outlook on the potential opportunities and technical challenges in this rapidly developing field.

Keywords: liquid crystal spatial light modulators; liquid crystal devices; structured light; holography; applications

Yang YQ, Forbes A, Cao LC. A review of liquid crystal spatial light modulators: devices and applications. *Opto-Electron Sci* **2**, 230026 (2023).

Introduction

The generic Gaussian beams produced by common lasers have limited appeal in fully meeting the growing needs of modern optical systems that seek to exploit full control over all degrees of freedom of light, now referred to as structured light[1–3]. Light shaping has a long history[4,5], dating back thousands of years with reflective elements[6], then refractive freeform elements[7], and later in the 1990s based on computer generated holograms (CGHs)[8] and diffractive optical elements (DOEs)[9–12], harnessing interference for light control. The field's recent explosion can be attributed to the on-demand rewritable solutions based on liquid crystal spatial light modulators (LC-SLMs), moving beyond display elements to sophisticated light structuring and control devices[13]. Although the underpinning technology can be traced back to the 1970s[14,15], several decades of extensive material research and development, device innovation, as well as heavy investment in advanced manufacturing technology, have brought LC-SLMs to the fore as an important tool in the field of optics and photonics[16–18]. This dynamic flat-panel optical device has gained increasing interest due to its attractive properties, such as phase-only modulation, photo-patternable characteristics, real-time input or output signals, high efficiency, polarization selectivity, the capability of performing dynamic switching, and its ultra-thin form factor[19,20]. These unique properties not only replace conventional optical devices with a digital equivalent, but also facilitate functionality beyond the textbook by modulating light beams

[1]Department of Precision Instruments, Tsinghua University, Beijing 100084, China; [2]School of Physics, University of the Witwatersrand, Wits, South Africa.

*Correspondence: A Forbes, E-mail: Andrew.Forbes@wits.ac.za; LC Cao, E-mail: clc@tsinghua.edu.cn

Received: 10 August 2023; Accepted: 22 September 2023; Published online: 26 October 2023

in space[21,22] and time[23–25].

LC-SLMs have enabled the development of extensive compact and lightweight optical components with electronic modulation capacity, and as a result, LC-SLMs have shown great potential in widespread applications, and have been crucial in quantum optics[26,27], microscopy[28], imaging[29,30], optical trapping and tweezers[31,32], materials processing[33] and holography[34]. For instance, LC-SLMs can be used as spatial filters, deflectors, beam splitters or optical interconnects. Besides, they can lend themselves to free-space communications and high-performance computing. In computational imaging, LC-SLMs switch the ghost imaging target with different polarizations of light, lending themselves to applications in optical communication, imaging technology and security. In quantum communication, combined with the technologies of optical vortex, LC-SLMs show good performance with high capacity and large bandwidth. Moreover, LC-SLMs are ideal elements for encrypted patterns because of the high precisions and the usage of multiple controlled parameters, which can increase the security level. In microscopy, LC-SLMs allow live and real-time microscopic imaging of biological samples. In material processing, high resolutions, small pixel pitches and low cost of LC-SLMs meet the requirement of generating structures of arbitrary complexity. In light field control, LC-SLMs can work as a powerful tool in optical tweezers and optical trapping for studies of life science, and particle physics. In holographic display, LC-SLMs are dynamically programmable with high resolution and decent performance in naked-eye 3D displays. In interferometry, LC-SLMs are ideal elements for measuring the phase profile of samples at the sub-wavelength resolution.

What these many applications illustrate is the universal nature of LC-SLMs as enabling devices, and their consequent stimulating and reforming nature of research across diverse application areas. In this review, we provide our perspective on this field by reviewing the working principles of liquid crystal, diffraction optics, the recent progress of LC-SLMs, and their role in modern photonic applications. For newcomers to the field, it is inspiring to study the methods using LC-SLMs in different fields, as they often shape the trend and pave the way for modern optical technology. For those looking to improve established frameworks or develop new methods with advanced LC-SLMs, it should be fruitful to study works that are targeted at the enhancement of existing or proprietary frameworks.

Liquid crystal devices

Liquid crystal cells

A liquid crystal is a phase between solid and liquid, simply defined as a liquid with molecules arranged regularly and possessing useful attributes based on the electro-optic birefringent effect, the twisted nematic effect and the hybrid field effect. The molecules are generally slender rods, shaped like cigars, with the long axis direction of each molecule roughly the same. Due to the anisotropy of liquid crystals, the dielectric constant, conductivity and refractive index are direction dependent. For liquid crystals with a positive dielectric anisotropy, the application of an electric field causes the long axis of the molecules to align along the direction of the field. This alignment induces a change in the refractive index, giving rise to the electro-optic birefringent effect. Conversely, in the case of liquid crystals with negative dielectric anisotropy, the alignment of the long axis of molecules is perpendicular to the applied electric field, resulting in an inverse refractive index change. The working principle of the electro-optic birefringent effect is shown in Fig. 1(a) and 1(b). No light is outputted when the voltage is off, while polarized light is outputted when the voltage is on. There is no birefringence effect when the polarization direction of the incident light is the same as or perpendicular to the long axis of the molecule near the incident plane. In the twisted nematic effect, the molecular orientations of the upper and lower crystal planes of the liquid crystal are different. The liquid crystal molecules can be divided into many thin layers, each with molecules of a similar orientation, changing from layer to layer. The resulting structure can make the polarization direction of linearly polarized light rotate. As shown in Fig. 1(c), for a liquid crystal with a twist angle of 90 degrees, the molecules rotate uniformly without an electric field. The twisted nematic effect appears when the electric field is introduced, since the molecules deviate from the original direction and align towards the electric field[35,36], as shown in Fig. 1(d). The hybrid field effect is the combination of electro-optic birefringent effect and twisted nematic effect. In the field of optical information processing, the control of phase, amplitude and polarization of optical beams by LC-SLMs are mainly realized through the hybrid field effects[37].

The core of the light-controlling ability of LC-SLMs lies in the liquid crystal itself, whose properties determine the optical functionality. There are multiple liquid

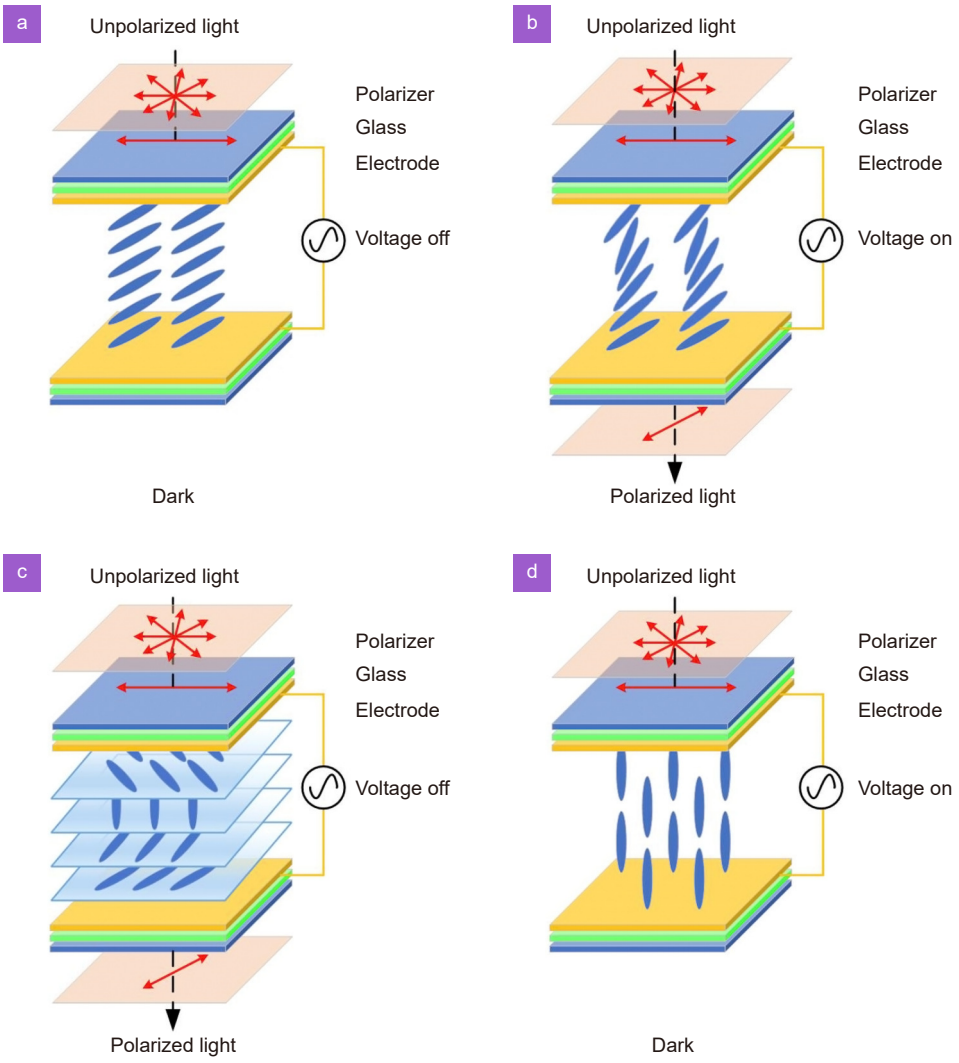

Fig. 1 | Working principle of liquid crystals. In the electro-optic birefringent effect, (**a**) no light is outputted when the voltage is off, while (**b**) polarized light is outputted when the voltage is on. In the twisted nematic effect, (**c**) the molecular orientations of the upper and lower crystal planes of the liquid crystal are different. Molecules rotate uniformly along the crystal direction without voltage. (**d**) Molecules deviate from the original direction and align towards the electric field when the voltage is on.

crystal cell structures and driving electrode configurations that can be employed for LC-SLMs. Examples include the vertical alignment liquid crystal cell (VA-LC Cell), in-plane switching liquid crystal cell (IPS-LC Cell), twisted nematic liquid crystal cell (TN-LC Cell), and super twisted nematic liquid crystal cell (STN-LC Cell). Without electric field, VA-LC cells and IPS-LC cells are uniform. In TN-LC cells, the vector of liquid crystal is twisted at approximately 90 degrees, while in STN-LC cells, the vector of liquid crystal is twisted at an angle larger than 90 degrees, such as 180 degrees, 240 degrees, or 270 degrees. Each cell comprises a 2D pixel array ($M\times N$) that can be electrically switched on or off. Each pixel is composed of a liquid crystal cell sandwiched between transparent electrodes. In the early stage, the TN-LC cell was driven by two groups of electrodes ($M+N$), utilizing the multiplexing technique. The advantage of multiplexing is that $M\times N$ pixels can be addressed using only $M+N$ electrical contacts, which significantly reduces the number of electrodes when M and N are in the order of 10^3, making it suitable for high-information-content applications. However, the simplicity of multiplexing leads to a degradation of the device performance, especially in terms of contrast and limited pixel resolution. The performance of TN-LC cells is later enhanced by a different driving technique that utilizes thin film transistor (TFT) arrays. In TFT arrays, each pixel has associated transistors, which significantly improves performance but also increases production costs. These LC configurations are mainly for amplitude modulations. For phase-only

modulation, homogeneous LC cells are commonly used[38], while TN cell can also work if the voltage is kept below the threshold[39]. In the following section, we discuss the operating principles of various liquid crystal cells and their transmission characteristics with or without voltage.

Vertical alignment liquid crystal cell (VA-LC Cell)

In the VA-LC cell, as illustrated in Fig. 2(a), each liquid crystal cell consists of two glass substrates with a spacing of 3–5 μm of liquid crystal material in between. A thin alignment layer is deposited on the inner surface of the substrate to ensure that the liquid crystal molecules are aligned vertically at the same time as the surface is projected to facilitate alignment. A transparent electrode, generally made of indium tin oxide (ITO), is deposited on the inner surface of the substrate for electrical connectivity. On the two outer surfaces of the substrate, polarizers are laminated to form an orthogonal polarizer. In a basic VA-LC cell with only one domain, the absorption axis of both polarizers can be aligned at a degree angle with the horizontal direction. Meanwhile, the liquid crystal is tilted in the *Y*-*Z* plane, and the structure is symmetrical in terms of apparent brightness. For a multi-domain cell, the absorption axis is often arranged in the horizontal direction and vertical direction, respectively. This arrangement of polarizers ensures the highest contrast in both directions. Under the application of an electric field, the liquid crystal molecules tilt at 45 degrees relative to the axes of the polarizer. As a result, the liquid crystal cell behaves as a half-wave plate with high transmission to crossed polarizers. The transmittance of light through the liquid crystal cell can be modulated by controlling the voltage.

In-plane switching liquid crystal cell (IPS-LC Cell)

The planar conversion mode of uniform parallel arrangement nematic liquid crystal cells was introduced in the mid-1990s as a means of improving viewing angles without the use of a thin film compensator. Figure 2(b) depicts the IPS model of a nematic liquid crystal cell that is sandwiched between two crossed polarizers, with one of the polarizers having a transmission axis parallel to the liquid crystal vector in the plane of incidence. When the incident light beam passes through the liquid crystal cell, only one mode of light waves, either ordinary or extraordinary, is excited, allowing the light waves to traverse the cell without experiencing any phase delay. When the electric field is off, the crossed polarizer configuration results in zero transmission. Under the application of an electric field to the liquid crystal cell in the *X*-*Y* plane, the liquid crystal molecules align in the direction of the field, the *Y*-axis, resulting in a distortion denoted by β in the *X*-*Y* plane. The distortion angle β in an IPS-LC cell varies as a function of position *Z* due to the boundary conditions of the liquid crystal molecules and the direction of friction. However, unlike a TN-LC cell, the distortion of the IPS-LC cell is not a linear function of position along the *Z*-axis. With the exception of a small pretilt, the tilt angle relative to the *Y* axis can be regarded as zero provided that the electric field is maintained within the plane.

Twisted nematic liquid crystal cell (TN-LC Cell)

The TN-LC cell is an important type of liquid crystal cell that differs from VA-LC and IPS-LC cells. In TN-LC, the cell is composed of a liquid crystal layer that is sandwiched between a pair of polarizers, with a twist angle of 90 degrees in total. TN-LC cells are widely used in notebook computers, calculators, and other small electronic devices due to their low power consumption, fast response time, and low cost. However, they have certain limitations such as narrow viewing angles and limited color reproduction compared to other liquid crystal modes. As illustrated in Fig. 2(c), each TN-LC cell is composed of a liquid crystal layer placed between two glass plates with a gap of 5–10 μm. An ITO conductive coating is deposited on the inner surface of the glass plates, and a thin layer of polyimide with a thickness of several hundred angstroms is applied to the electrode surface. The polyimide film is wiped unidirectionally to ensure its direction is parallel to the wiping direction on the surface. In 90-degree TN, the wiping direction of the lower substrate is perpendicular to the wiping direction of the upper surface. Consequently, the liquid crystal vectors of the area between the glass plates undergo a continuous and uniform distortion of 90 degrees without voltage. A sheet polarizer is laminated on the outer surface of the glass plate, and its transmission axis is set parallel to the wiping direction of the adjacent polyimide film. When a small voltage is applied to the electrode, e.g., 3–5 V, a strong electric field is generated in the liquid crystal. The dielectric anisotropy of the liquid crystal causes it to align with the direction of the applied electric field, resulting in a vertical arrangement of liquid crystal molecules. The vector of the liquid crystal is perpendicular to the panel, which is the C-plate of the

liquid crystal. When light propagates along the vertical direction of the C-plate, the polarization plane remains unchanged. When the C-plate is placed between a pair of orthogonal polarizers, it leads to zero transmittance. Thus, the transmittance of light through the liquid crystal cell can be controlled by adjusting the voltage.

Super twisted nematic liquid crystal cell (STN-LC Cell)

When a voltage is applied to the liquid crystal cell, the orientation of liquid crystal molecules changes in response to the electric field. The orientations of these molecules in the liquid crystal cell are determined by the

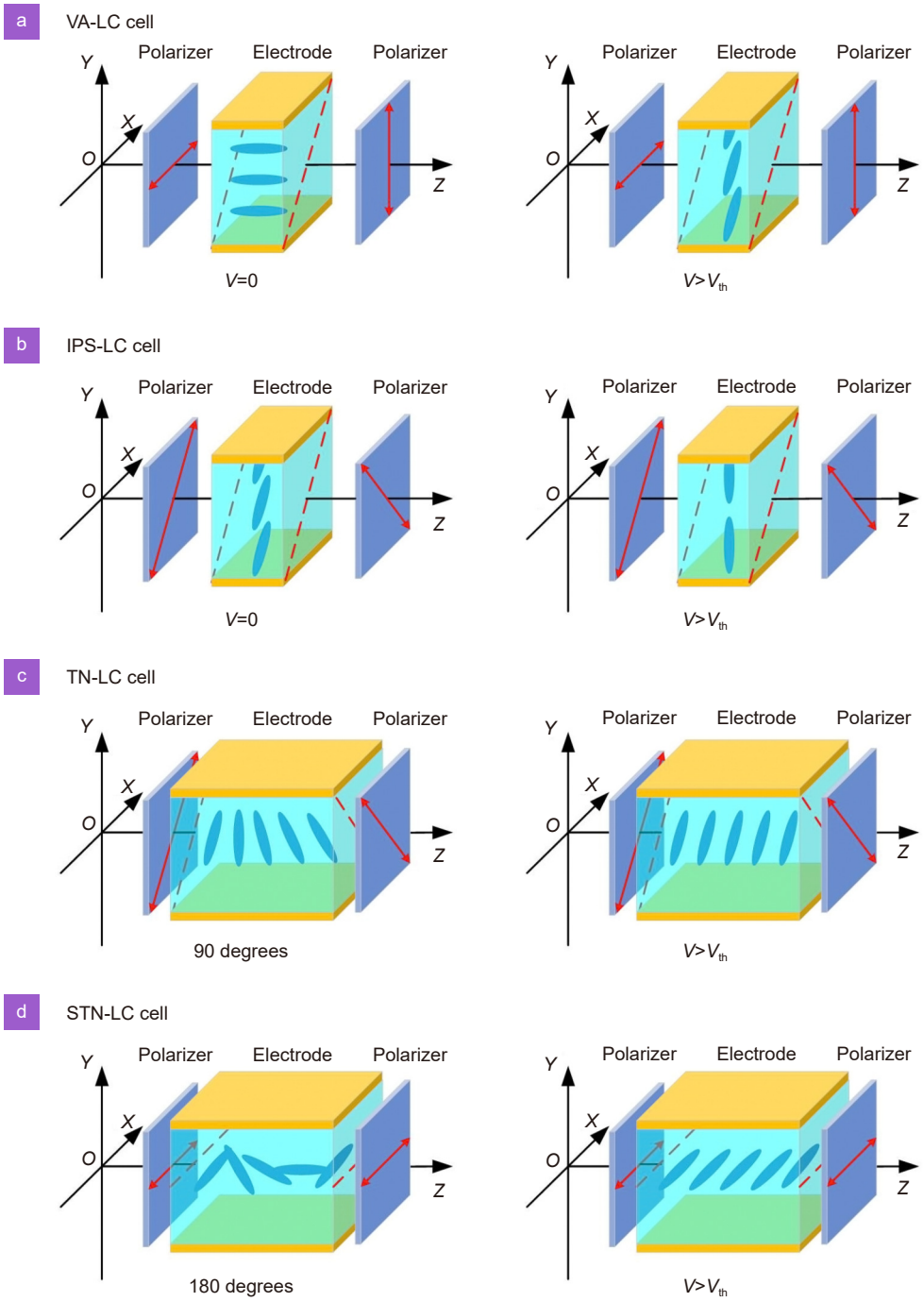

Fig. 2 | Models of liquid crystal cells. (**a**) Model of VA-LC cell. Under the application of an electric field, the liquid crystal molecules tilt at 45 degrees relative to the axes of the polarizer. (**b**) Model of IPS-LC cell. Under the application of an electric field to the liquid crystal cell in the *X*-*Y* plane, the liquid crystal molecules align in the direction of the field. (**c**) Model of TN-LC cell with a twist angle of 90 degrees in total. The liquid crystal vectors of the area between the glass plates undergo a continuous and uniform distortion of 90 degrees without voltage. (**d**) Model of STN-LC cell with a twist angle of 180 degrees in total. *V* represents the voltage, V_{th} represents the threshold voltage of the liquid crystal cell.

balance between elastic energy and electrostatic energy. The change in orientation results in a change in the transmittance of the liquid crystal cell. Typically, the display panel is composed of a 2D array of liquid crystal pixels, which is $M \times N$, with each pixel being a small liquid crystal cell that can be electrically turned on or off. To achieve this, it is necessary to electrically position each individual liquid crystal cell, which can be achieved using multi-channel circuit technology requiring only $M + N$ electrodes. However, due to crosstalk, the voltage difference between on and off in each liquid crystal cell cannot be too large, limiting the contrast of the display. To address this issue, the STN-LC cell is developed. By applying an appropriate voltage, the liquid crystal vector in the STN-LC cell is effectively distorted or redistributed, resulting in high contrast. Figure 2(d) depicts the molecular orientations of the STN-LC cell with a twist angle of 180 degrees in total. The high contrast is achieved by distorting or redistributing the liquid crystal vectors in the liquid crystal cell under an appropriate external voltage.

Advances in LC-SLMs

When the aforementioned cells are arranged together on a one-dimensional or two-dimensional plane, they form an LC-SLM device. By designing the shape, size, position and orientation of the unit structures, LC-SLMs can modulate the optical parameters, e.g., amplitude, phase and polarization of the incident light wave in an arbitrary manner. This unique ability of modulation with multi-degree of freedom allows for the replacement of traditional optical elements with bulky structures and single functionality, making the LC-SLMs lightweight, ultrathin, and multifunctional devices[40,41]. In addition, LC-SLMs are compatible with semiconductor manufacturing techniques, enabling mass production and manufacturing. LC-SLMs have obvious advantages in the lightweight and integration of photoelectric systems, and they show great potential in the fields of high-end equipment, aerospace and electronics. With the continuous advancements in material research and significant investments in advanced manufacturing technologies, the performances of LC-SLMs have significantly improved, as shown in Fig. 3. These improvements have led to a decrease in the pixel pitch to the micron level and an increase in the number of pixels to tens of millions. Compound Photonics and Himax have demonstrated SLMs with a pixel pitch of about 3 μm and 4.25 μm[42]. Today, high-performance LC-SLM devices are available commercially, and Table 1 provides a summary of the state-of-the-art LC-SLMs that are currently available in the market.

Large-aperture liquid crystal devices have emerged as a significant area of research and technological innovation within the field of optics[43,44]. These devices leverage the unique properties of liquid crystals, such as the tunable refractive index and responsiveness to external electric fields, to create versatile and dynamically controllable optical components. The potential of large aperture liquid crystal devices lies in the ability to manipulate light across a broad spectral range. This makes them particularly valuable for various applications, ranging from beam shaping to adaptive optics. Their dynamic tunability allows for real-time adjustments in response to changing environmental conditions or specific operational requirements.

Shaping light by diffraction

While research devices are capable of controlling light by geometric phase[45,46], they are not yet commercially available, and thus, most commercial LC-SLMs available today modulate only the dynamic (or propagation) phase of the light. This phase-only functionality can be exploited for control of many degrees of freedom, extending to amplitude modulation and polarization modulation. As the liquid crystals in each cell are rotated, the local refractive index $n(x,y)$ changes, resulting in a phase change across the device given by $\Phi_{\mathrm{SLM}}(x,y) = kn(x,y)d$, where k is the wavenumber of the light and d is the thickness of LC cell. The question is how to use this phase change as a means to control and shape light. The answer lies in the notion of diffraction. Diffraction is a fundamental optical phenomenon that accounts for many phenomena that cannot be explained by geometrical optics, such as the bending and spreading of the light. Early optical elements were designed based on refraction and reflection, where diffraction was considered a hindrance. However, the advent of fast computers and modern lithography meant that optical elements could be designed and fabricated to exploit diffraction and interference. Such diffractive optical elements (DOEs), either as smooth kinoforms or binary equivalents, have given birth to a myriad of new optical functionalities, such as pattern generators, beam shapers, and gratings, all utilizing a surface relief profile with a depth on the order of the wavelength of the light. As a consequence, DOEs are

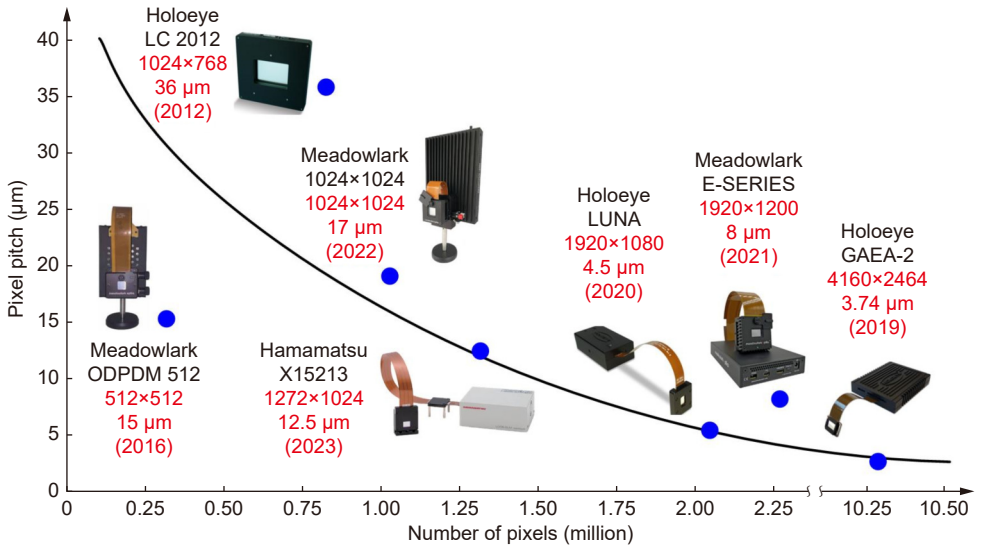

Fig. 3 | The performances of LC-SLMs have significantly improved with continuous advancements in material research and significant investments in advanced manufacturing technologies. These led to a decrease in the pixel pitch to the micrometer level and an increase in the number of pixels to tens of millions.

Table 1 | Performances of commercially available spatial light modulators.

Company model	Resolution	Pixel pitch	Fill factor	Wavelength range (nm)
Holoeye GAEA-2	4160×2464	3.74 μm	90%	420–1100
Holoeye LUNA	1920×1080	4.5 μm	91%	420–1100
Hamamatsu X15213-01	1272×1024	12.5 μm	96.8%	400–700
Meadowlark 1024×1024	1024×1024	17 μm	97.2%	500–1200
Meadowlark E-SERIES	1920×1200	8 μm	95.6%	500–1200
Meadowlark ODPDM512	512×512	15 μm	83.4%	400–1650
Holoeye LC2012	1024×768	36 μm	58%	400–800
Meadowlark HSP12K	1×12288	1.6 μm×19.66 mm	100%	400–1650

typically much thinner and lighter than conventional refractive elements, making them an attractive replacement in a number of applications. In the context of this review, we can treat the LC-SLM as a pixelated DOE that is rewritable, so that all the theory related to DOEs can be translated to LC-SLMs. For instance, the fundamental equation governing diffraction off a periodic structure indicates that light will emerge at diffraction angles θ satisfying

$$m\lambda = p\sin(\theta)\ , \tag{1}$$

where m is the diffraction order, λ is the wavelength and p is the grating pitch. This tells us *where* the light will be diffracted, which can be useful for various applications. For instance, in a holographic display system, the viewing angle is double the maximum diffraction angle. In order to display a 3D image with a wide angle of view, an LC-SLM's pixel pitch has to be sufficiently smaller than the wavelength. However, even with the finest 8K LC-SLM with a pixel pitch of 3.5 μm, the viewing angle is limited to about 10 degrees. The diffraction equation only provides information on the direction of diffracted light, but *how much* light will be going in a particular direction. The answer to this, the diffraction efficiency, depends largely on the type of periodic structure (binary, blazed, sinusoidal, etc.) whereas the function of the element depends largely on the spacing of the pitch in space, e.g., $p(x,y)$. For instance, the diffraction efficiency for a 2^N level binary function is given by

$$\eta = \left[\frac{\sin\left(\pi m/2^N\right)}{\pi m/2^N}\right]^2\ , \tag{2}$$

where η is the power into the m order, and the non-zero orders are given by $m = qN+1$ where q is any integer.

What remains is to determine *what* the light looks like. Diffraction can be divided into two categories, analytic diffraction and numeric diffraction. Analytic diffraction is designed based on ray tracing, as the phase profile can be defined analytically on an infinitely thin interface. Examples of typical analytic elements include

lenses, gratings, and interferograms, which may be a single element or in combination with refraction or reflection elements to create a hybrid optical system. On the other hand, numeric diffraction is calculated iteratively as a black box. The incoming wavefront and the desired output wavefront are specified, with the incoming wavefront being a particular amplitude or phase function, and the output field being an amplitude-only function located either in the far field or near field. Iterative algorithms are then used to reduce the specific cost of the diffraction efficiency in a given order, such as reconstruction uniformity, signal-noise-rate, or root-mean-square error between a desired reconstruction and an actual reconstruction. Examples of typical numeric elements include diffusers, beam splitters, beam shapers, CGHs, Fourier filters, spot array generators, and so on. As shown in Fig. 4(a) and 4(b), LC-SLM can replace typical analytic and numeric elements to realize the modulation of the light field in amplitude, phase and polarization. Holograms on LC-SLMs can be designed or calculated analytically, whereas numeric diffraction requires numeric optimization through iterative algorithms since there is no analytical solution to the diffraction problem. Depending on the input wavefront and the signals provided by the computer, LC-SLMs can produce various types of beams and images, either as single or compound images. In this section, we are interested in structured light, and so we briefly cover the common beam types that are typically created by LC-SLMs. Apparatus of LC-SLM and SLM holograms that produce different types of beams are illustrated in Fig. 4(c) and 4(d), illustrating the diverse capabilities of this technology.

Bessel beams

Bessel beams have a transverse intensity profile according to the family of Bessel functions[47]. A zeroth-order Bessel beam has a transverse intensity profile with a bright central core surrounded by bright concentric rings. Unlike Gaussian beams, a Bessel beam has a transverse intensity profile that does not spread as it propagates over a finite distance. Bessel beam can reconstruct around obstructions placed in the beam path, which makes Bessel beam useful for stacking multiple objects along the beam's central core. Bessel beams are exact solutions to the free-space Helmholtz wave equation in cylindrical symmetry and are mathematically given by

$$E(\rho,\varphi,z) = E_0 \mathrm{J}_l(k_t\rho)\exp(\mathrm{i}l\varphi)\exp(k_z z)\ , \tag{3}$$

where ρ and φ denote the polar coordinates, z denotes the axial coordinate, J_l is the Bessel function of order l, k_t is the transverse component of the wave vector $\boldsymbol{k}$, and k_z is the longitudinal component of the wave vector $\boldsymbol{k}$.

The two common methods to generate Bessel beams are based on a conical lens (axicon) for near-field creation, and a ring aperture (annular slit) for far-field creation. Even though both can be encoded as a hologram on the SLM, the former is more efficient. The transfer function of an axicon is described by

$$t(\rho,\varphi) = \exp(\mathrm{i}k_t\rho)\ . \tag{4}$$

The transverse component of the wave vector k_t can be expressed in terms of the angle α of the axicon as

$$k_t = \alpha(n-1)k\ , \tag{5}$$

where n is the refractive index of the axicon. Bessel-Gauss beams generated in the laboratory are Bessel beam enveloped with a Gaussian beam of radius w_0 and thus have a finite propagation distance described by

$$z_{\max} = w_0\frac{k}{k_t}\ . \tag{6}$$

By adding the term $\exp(\mathrm{i}l\varphi)$ to Eq. (3), we can get the transfer function of a high-order Bessel beam, which is given by

$$t(\rho,\varphi) = \exp[\mathrm{i}k\alpha(n-1)\rho]\exp(\mathrm{i}l\varphi)\ . \tag{7}$$

Thus, the mathematical expression to generate a phase hologram for the SLM with the above transfer functions takes the form of

$$\begin{aligned}\Phi_{\mathrm{SLM}}(x,y) = \ &\mathrm{mod}\left[k\alpha(n-1)\sqrt{x^2+y^2}\right.\\ &\left.+\,l\arctan(y/x)+2\pi(G_x x+G_y y),2\pi\right]\ .\end{aligned} \tag{8}$$

Finite-energy Airy beams

Another solution to the paraxial wave equation is given in terms of the Airy functions, which are called Airy beams[48]. The mathematical expression for these beams is given by

$$\begin{aligned}A(s_x,s_y,\xi) =& A_i\left[s_x-\left(\frac{\xi}{2}\right)^2\right]A_i\left[s_y-\left(\frac{\xi}{2}\right)^2\right]\\ &\cdot\exp\left[\frac{\mathrm{i}\xi}{2}\left(s_x+s_y-\frac{\xi^3}{3}\right)\right]\ ,\end{aligned} \tag{9}$$

where A_i is the Airy function, $s_x = x/x_0$ and $s_y = y/y_0$ represent dimensionless transverse coordinates, x_0 and y_0 are the transverse scale parameters, $\xi = z/kx_0^2$ is a normalized propagation distance. By imposing certain restrictions to Eq. (9), a very good approximation to the ideal Airy beam can be realized in the optical regime, described by

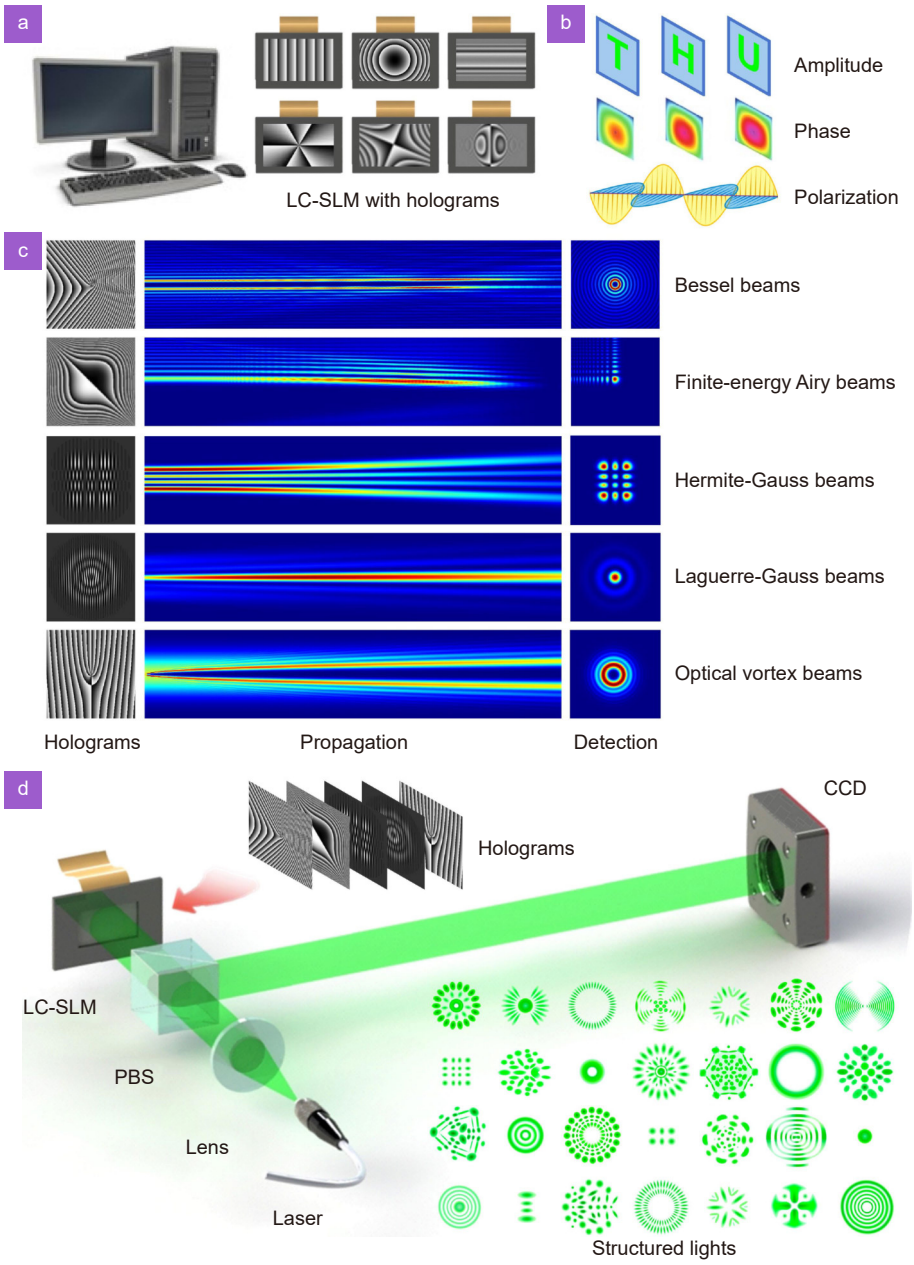

Fig. 4 | Apparatus of LC-SLM and SLM holograms that produce different types of beams. (**a**) LC-SLM can be designed or calculated to replace typical analytic and numeric elements to realize the modulation of the light field in (**b**) amplitude, phase and polarization. (**c**) Various types of beams, such as Bessel beams, finite-energy Airy beams, Hermite-Gauss beams, Laguerre-Gauss beams, and optical vortex beams, can be obtained by uploading holograms into the LC-SLM. (**d**) Different types of structured lights detected by a CCD.

$$A\left(s_x, s_y, \xi = 0\right) = A_i\left(s_x\right) A_i\left(s_y\right) \exp\left[b\left(s_x + s_y\right)\right] , \quad (10)$$

where b is a positive parameter, typically smaller than one that limits the energy of the Airy beam. The final expression for this "finite-energy Airy beam" is described by

$$A\left(s_x, s_y, \xi\right) = A_i\left[s_x - \left(\frac{\xi}{2}\right)^2 + \mathrm{i}b\xi\right] A_i\left[s_y - \left(\frac{\xi}{2}\right)^2 + \mathrm{i}b\xi\right]$$
$$\cdot \exp\left[b\left(s_x + s_y\right) - b\xi^2 + \mathrm{i}b\xi^2 - \frac{\xi^3}{6} + \frac{\mathrm{i}\xi\left(s_x + s_y\right)}{2}\right] . \quad (11)$$

For the finite energy, Airy beam maintains its non-diffractive properties over a finite distance only.

The experimental generation of these beams can be achieved by encoding a hologram corresponding to the inverse Fourier transform of A_0. The phase encoding on the SLM is described by

$$\Phi_{\mathrm{SLM}}\left(x, y\right) = \mathrm{mod}\left[\frac{x^3 + y^3}{3}, 2\pi\right] . \quad (12)$$

Hermite-Gauss beams

Hermite-Gauss modes are a set of solutions to the paraxial wave equation in Cartesian coordinates[49]. The mathematical representation is given in terms of a Gaussian function and the Hermite polynomial $H_n(x)$ as

$$HG_{nm}(x,y,z) = \frac{1}{w(z)}\sqrt{\frac{2^{1-n-m}}{\pi n!m!}}H_n\left[\frac{\sqrt{x}}{w(z)}\right]H_m\left[\frac{\sqrt{y}}{w(z)}\right] \cdot \exp\left[\mathrm{i}(n+m+1)\xi(z)\right]\exp\left[-\left(\frac{\rho}{w(z)}\right)^2\right] \cdot \exp\left(-\frac{\mathrm{i}k\rho^2}{2R(z)}\right)\exp(-\mathrm{i}kz)\ , \tag{13}$$

where n and m are the positive integers. Other parameters are described by

$$\rho = \sqrt{x^2+y^2}\ , \tag{14}$$

$$w(z) = w_0\sqrt{1+\left(\frac{z}{z_\mathrm{R}}\right)^2}\ , \tag{15}$$

$$R(z) = z\left[1+\left(\frac{z_\mathrm{R}}{z}\right)^2\right]\ , \tag{16}$$

$$w_0 = z\sqrt{\frac{\lambda z_\mathrm{R}}{\pi}}\ , \tag{17}$$

$$\xi(z) = \arctan\left(\frac{z}{z_\mathrm{R}}\right)\ . \tag{18}$$

Equation (13) represents a paraboloidal wave with the radius of curvature $R(z)$, beam waist w_0, and beam size $w(z)$. z_R is a constant known as the Rayleigh range, which is used to measure the distance over which the beam remains well collimated. $\xi(z)$ is an additional phase shift that the wavefront acquires upon propagation through the beam waist, which is known as the Gouy phase.

Hermite-Gauss beams can be generated by employing complex amplitude modulation. The amplitude term and the phase term are given by

$$A_\mathrm{HG}(x,y,z) = \frac{1}{w(z)}\sqrt{\frac{2^{1-n-m}}{\pi n!m!}}H_n\left[\frac{\sqrt{x}}{w(z)}\right] \cdot H_m\left[\frac{\sqrt{y}}{w(z)}\right]\exp\left[-\left(\frac{\rho}{w(z)}\right)^2\right]\ , \tag{19}$$

$$\Phi_\mathrm{HG}(x,y,z) = \exp\left[\mathrm{i}(n+m+1)\xi(z)\right] \cdot \exp\left(-\frac{\mathrm{i}k\rho^2}{2R}\right)\exp(-\mathrm{i}kz)\ . \tag{20}$$

Thus, the encoded hologram takes the form of

$$\Phi_\mathrm{SLM} = f_\mathrm{HG}\cdot\sin\left(\Phi_\mathrm{HG}+G_x x+G_y y\right)\ , \tag{21}$$

where f_HG is the amplitude phase function and can be found numerically from the relation

$$J_1(f_\mathrm{HG}) = A_\mathrm{HG}\ . \tag{22}$$

Laguerre-Gauss beams

Laguerre-Gauss modes are another solution to the paraxial Helmholtz equation in cylindrical coordinates[50]. They are mathematically described by

$$LG_p^l(\rho,\varphi,z) = \frac{w_0}{w(z)}\sqrt{\frac{2p!}{\pi(|l|+p)!}}\left[\frac{\sqrt{2}\rho}{w(z)}\right]^{|l|} \cdot L_p^l\left[2\left(\frac{\rho}{w(z)}\right)^2\right]\exp\left[\mathrm{i}(2p+|l|+1)\xi(z)\right] \cdot \exp\left[-\left(\frac{\rho}{w(z)}\right)^2\right]\exp\left(-\frac{\mathrm{i}k\rho^2}{2R}\right)\exp(-\mathrm{i}l\varphi)\ , \tag{23}$$

where L_p^l is the Laguerre function and the rest of the parameters are the same as in the HG_{nm} modes.

Laguerre-Gauss beams generated by SLMs are approximated using complex amplitude modulation. The amplitude term and the phase term are given by

$$A_\mathrm{LG} = \frac{w_0}{w(z)}\sqrt{\frac{2p!}{\pi(|l|+p)!}}\left[\frac{\sqrt{2}\rho}{w(z)}\right]^{|l|}L_p^l\left[2\left(\frac{\rho}{w(z)}\right)^2\right] \cdot \exp\left[-\left(\frac{\rho}{w(z)}\right)^2\right]\ , \tag{24}$$

$$\Phi_\mathrm{LG} = \exp\left[\mathrm{i}(2p+|l|+1)\xi(z)\right] \cdot \exp\left(-\frac{\mathrm{i}k\rho^2}{2R}\right)\exp(-\mathrm{i}l\varphi)\ . \tag{25}$$

Thus, the encoded hologram has the form of

$$\Phi_\mathrm{SLM} = f_\mathrm{LG}\cdot\sin\left(\Phi_\mathrm{LG}+G_x x+G_y y\right)\ , \tag{26}$$

where f_LG is obtained by numerical evaluation

$$J_1(f_\mathrm{LG}) = A_\mathrm{LG}\ . \tag{27}$$

Optical vortex beams

Vortex beams carry orbital angular momentum (OAM) by virtue of a helical twist to the wavefront, characterized by a phase function of the form of $\exp(-\mathrm{i}l\phi)$, resulting in photons with $l\hbar$ of OAM[51]. We have already seen that Bessel beams and Laguerre-Gauss beams have this form, but these are only two such examples. Ignoring the amplitude function, the desired phase profile can be experimentally generated with an SLM by encoding an azimuthal variation and blazed grating to separate the first order from the others. The phase encoding on the SLM is described by

$$\Phi_{\mathrm{SLM}} = \mathrm{mod}\left[l\phi + 2\pi\left(G_x x + G_y y\right), 2\pi\right] . \qquad (28)$$

Applications of LC-SLMs

The unique properties of LC-SLMs make them well-suited for use as dynamic optical devices, which can replace conventional optical devices with a digital equivalent and also facilitate new functionality. In this section, we review the significant progress that has been made in the applications of LC-SLMs. The diverse range of these applications is captured in Fig. 5, including beam shaping and steering, holography, optical trapping and tweezers, measurement, wavefront coding, optical vortex, quantum applications, and more. We focus on revealing the unique dynamic flat-panel functionalities of the LC-SLMs.

Beam shaping and steering

Shaping the light field by changing its phase or intensity has enabled significant advances in optics. Refractive and reflective elements, such as lenses, prisms, and mirrors, are common devices for beam shaping and steering by deflecting the light paths. Elements that work with this diffraction effect are called DOEs. The propagating phase of light changes when it passes through the micro-structure pattern made on a substrate material. DOEs have become the first choice in many applications due to their flexible plasticity, absolute angular accuracy at designed wavelengths, small size, and flatness. However, LC-SLMs can change the phase pixel by pixel for the laser beam, and thus can replace traditional beam shaping and steering DOEs. Previous works have realized continuous phase and binary intensity modulation of beams with the help of beam shaping techniques based on LC-SLMs[52–57]. Dispersion-free beam shaping has been achieved through the intermediate transversal light beam magnification, which balances the mismatch in the grating constants and leads to total residual angular dispersion compensation.

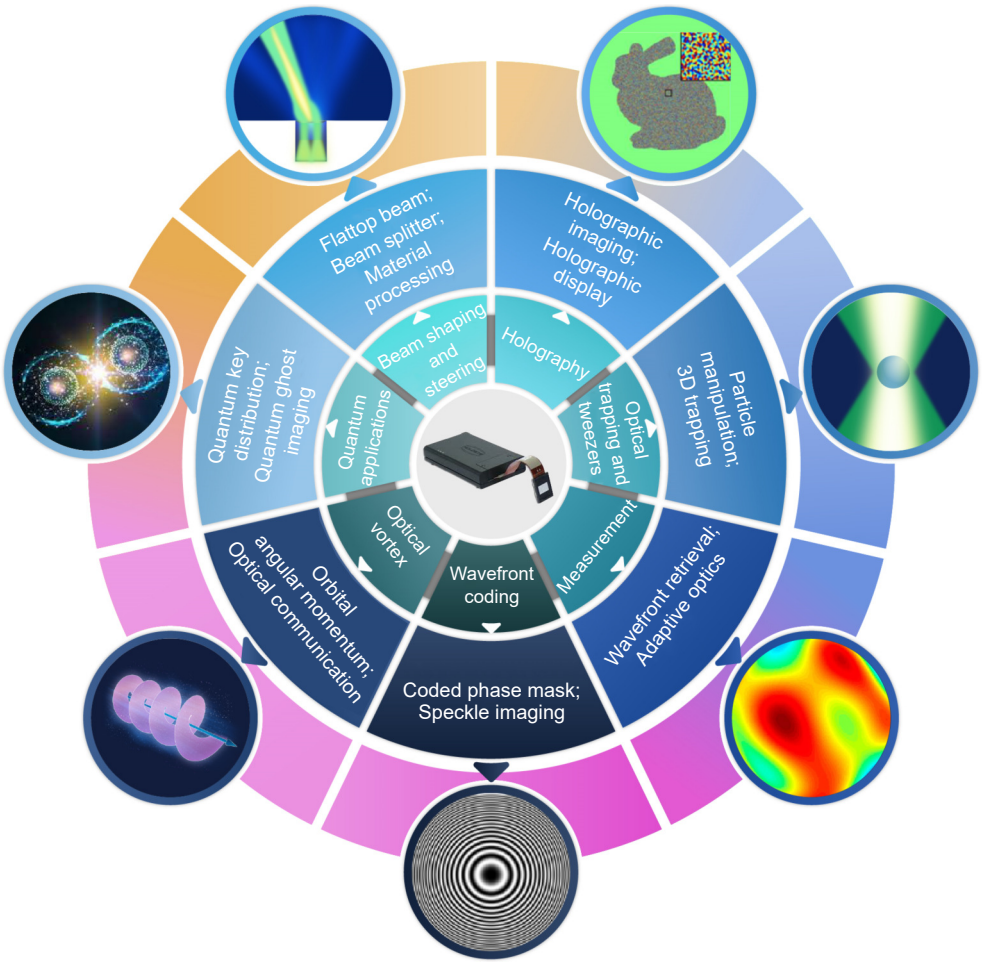

Fig. 5 | LC-SLMs are versatile and powerful devices that find diverse applications, including beam shaping and steering, holography, optical trapping and tweezers, measurement, wavefront coding, optical vortex, and quantum applications. The unique properties, such as high resolution, high speed, and dynamic control, make them well-suited for use as dynamic optical devices in a wide range of applications.

LC-SLMs have also been used to achieve white light beam shaping[58] and axial sub-Fourier focusing of optical beams[59]. In this approach, the generated beams have an axial focusing that is narrower than the Fourier limit. The generated beams are constructed from the superposition of Bessel beams with different longitudinal wave vectors, which realizes a super oscillatory axial intensity distribution. In beam steering, LC-SLMs enable the generation of dynamic gratings to steer the beam toward a specific direction or for beam scanning. Multifocal arrays have attracted considerable attention for their potential applications in parallel optical tweezers, parallel recording, and multifocal multiphoton microscopy. Methods of generating 3D dynamic and controllable multifocal spots in the focal volume of the objects have been proposed[60]. Specifically, T. Zeng et al proposed a specific pseudo-period encoding technique to create 3D vectorial multifocal arrays with the capability of manipulating the position, intensity and polarization state of each focal spot, as shown in Fig. 6(a)[61]. The experiment demonstrates that the vectorial multifocal arrays have a tunable position and polarization state with high quality.

Beam shaping and steering techniques find wide applications in several domains, such as focusing light into materials or turbid media[62–64], measuring the transmission matrix in disordered media[65] or opaque materials[66], optimizing and characterizing optical properties[67–72], laser printing[73,74], manufacturing equipment[75], detecting beams[70,76], material processing[77–81], etc. Material processing utilizes beams projected onto the surface of the material to induce thermal effects for processing, including laser welding, cutting, marking, drilling, and micromachining. Among the techniques for generating structures of arbitrary complexity with sub-micrometer resolution and high efficiency, photopolymerization stands out as a powerful method. It allows for the simultaneous building of structures with diffractive patterns instead of multidimensional scanning of a single focus. Micro-supercapacitors, a promising miniaturized energy storage device, suffer from inefficient microfabrication technologies and low energy density, thus limiting their range of applications. Y. Yuan et al proposed a flexible and designable micro-supercapacitor, fabricated through a single pulse laser photonic-reduction stamping technique, as shown in Fig. 6(b)[82]. This unique technique has the potential to overcome the limitations of low energy density and high-throughput fabrication of micro-supercapacitors, thereby expanding their range of applications.

Holography

Since Gabor invented holography, the field of holographic imaging and display has grown with the increasing use of LC-SLMs. A hologram is an interference recording of a 3D surface by calculating in reverse from the target image. Upon proper recording, reconstruction, and viewing conditions, unlike traditional 2D photography, the image appears to be 3D again. LC-SLMs are non-mechanical programmable wavefront modulation devices that introduce diversity into the image data. Three different techniques of single channel digital holography are discussed, including the joint object reference digital interferometer (JORDI), Fresnel incoherent correlation holography (FINCH) and Fourier incoherent single channel holography (FISCH)[83]. Pixelated LC-SLMs can be implemented to encode complex modulation by means of appropriate CGHs, enabling the synthesis of fully complex fields with high accuracy. Methods of realizing hologram generation with maximum reconstruction efficiency, optimum bandwidth and high signal-to-noise ratio in CGH have been proposed[84–89], as shown in Fig. 7 . Y. Zhao et al proposed a novel layer-based angular spectrum method of CGH, as shown in Fig. 7(a)[88]. Experimental results show that the proposed method can perform high-quality optical reconstructions of 3D scenes with dramatically reduced computational load and precise depth performance. X. Sui et al realized complex amplitude modulation through spatiotemporal double-phase hologram[90]. The method makes spatiotemporal double-phase holograms an appropriate way to digitally modulate static and quasi-static complex fields using existing LC-SLMs. In addition to the pure phase-based holography, LC-SLMs can realize amplitude or complex amplitude-based holography. This expanded capability allows for more versatile and sophisticated holographic applications, where both the phase and amplitude of light can be precisely manipulated to create complex and realistic holographic reconstructions.

Holographic displays have emerged as a powerful tool for constructing high-resolution and realistic 3D images, without the need for special glasses. Holography display techniques play a central role in diverse fields, such as scientific visualization, multimedia display, virtual reality, education and interactive designs. However, there is still a long way to go to improve it further. A material that takes all the advantages of holography does not exist. The performance characteristics of different materials have been analyzed to determine the advantages and

limitations of different approaches[91]. Various methods have been proposed to accelerate the generation of color holograms[92–94], reduce speckle noise[95,96], and implement time multiplexing[97]. Additionally, researchers are exploring various algorithms and techniques to improve display properties[98–102]. Optical see-through holographic near-eye displays have also been improved towards compactness, lightweight, low cost, and free of accommodation-convergence discrepancy[100,103,104]. Recent progress in photo-electronic techniques and devices has enabled the real-time display of 3D images in free space, including the extraction of all depth cues such as motion parallax, occlusion, and ocular accommodation. Researchers have made significant strides in improving image quality while maintaining image size[105], implementing holograms with high contrast and per-pixel focal control[106], reconstructing high-definition 3D fields[107], and handling holographic images in real time[108].

Optical trapping and tweezers

Optical trapping and tweezers are tools that utilize highly focused laser beams to exert a micro force on microscopic dielectric objects, enabling physical manipulation, holding, and repulsion of the material. These techniques have become valuable tools in a wide range of applications, including trapping or manipulating cells and cell components[109–117], measuring the interaction forces and hydrodynamics[118–122], measuring the fluid flow[123,124], and assembly of micro-structures[125,126]. However, precise spatial and temporal manipulation of multiple traps and independent manipulation of trapped micro-particles remains a challenging task in many applications. To address this, holographic or diffractive optical elements are widely implemented with LC-SLMs to form optical traps in multiple shapes[127–131], arbitrary arrays of traps or atoms[132,133], and unique trapping structures[134–137]. Typical applications of LC-SLMs in optical trapping and tweezers

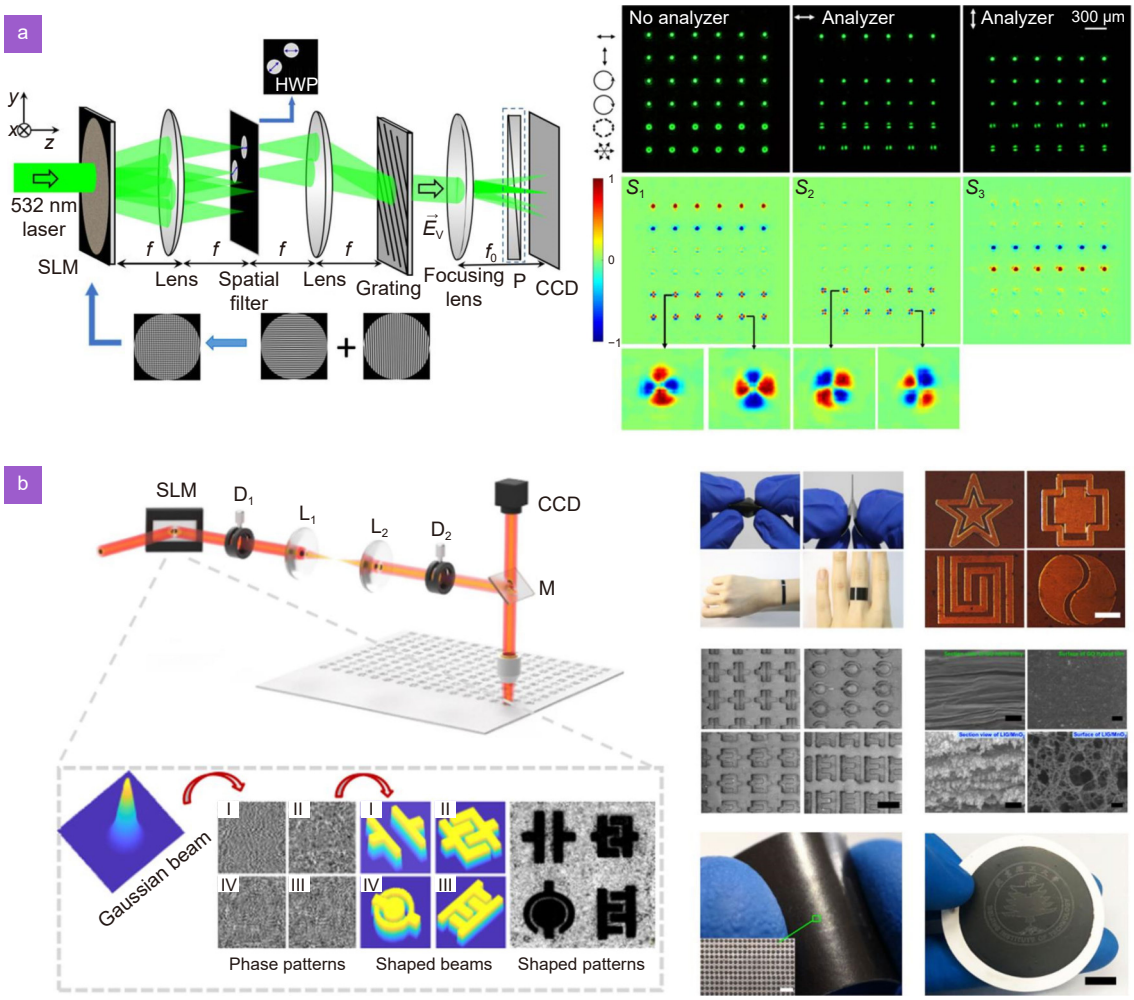

Fig. 6 | Applications of LC-SLMs in beam shaping and steering. (**a**) Generating 3D vectorial multifocal arrays by pseudo-period encoding. (**b**) Ultrafast fabrication of micro-supercapacitors using laser photonic-reduction stamping. Figure reproduced with permission from: (a) ref.[61], IOPscience; (b) ref.[82], Springer Nature.

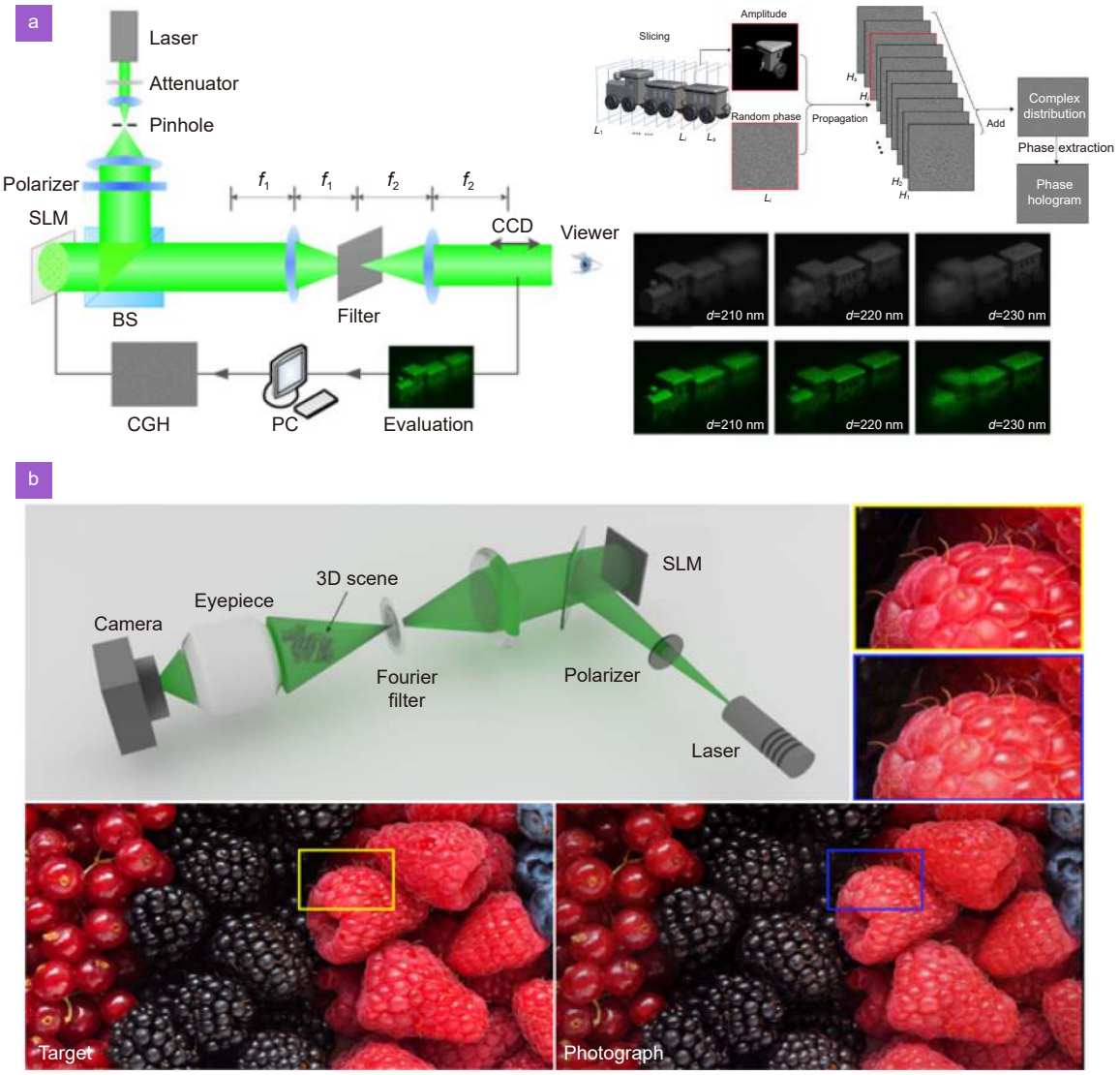

Fig. 7 | Applications of LC-SLMs in holography. (**a**) High-accuracy generation of CGHs by angular-spectrum layer-oriented method. (**b**) Real-time photorealistic 3D holography with deep neural networks. Figure reproduced with permission from: (a) ref.[88], OSA Publishing; (b) ref.[89], Springer Nature.

are shown in Fig. 8. In the field of quantum computation, quantum simulation and quantum many-body physics, it is essential to build a scalable neutral-atom platform. Optical trapping of atoms enables the construction and manipulation of quantum systems. To this end, H. Kim et al proposed a novel LC-SLM method to transport single atoms in real time with holographic micro-traps[132]. The method accomplished a 99% success rate for single-atom rearrangements for up to 10 mm translation. The technique can be further improved through increasing the number of atoms and initial loading efficiency. The application is not restricted to the preparation of an array, but can also be applied to many-body physics with ordered atoms and coherent qubit transports.

The use of optical tweezers has revolutionized the field of micro-manipulation by enabling the trapping, assembling, and sorting of multiple particles in 3D[111,135,138]. The inception of optical tweezers dates back to 1986[139]. Intensity-modulated patterns projected by an LC-SLM enable the manipulation of microparticles dynamically. Typical setups for optical tweezers involve on-axis Fourier holograms. However, an advanced optical setup has been proposed that uses an off-axis Fresnel hologram, which increases the flexibility of diffractively steered optical tweezers[140]. Rapid generation and analysis of optical tweezers meet the demand for development[141,142]. The advantage of optical tweezers is that it is possible to design any potential for the atom. The use of LC-SLMs in the design of arbitrary potentials has made optical tweezers a powerful tool in life science, material science, and

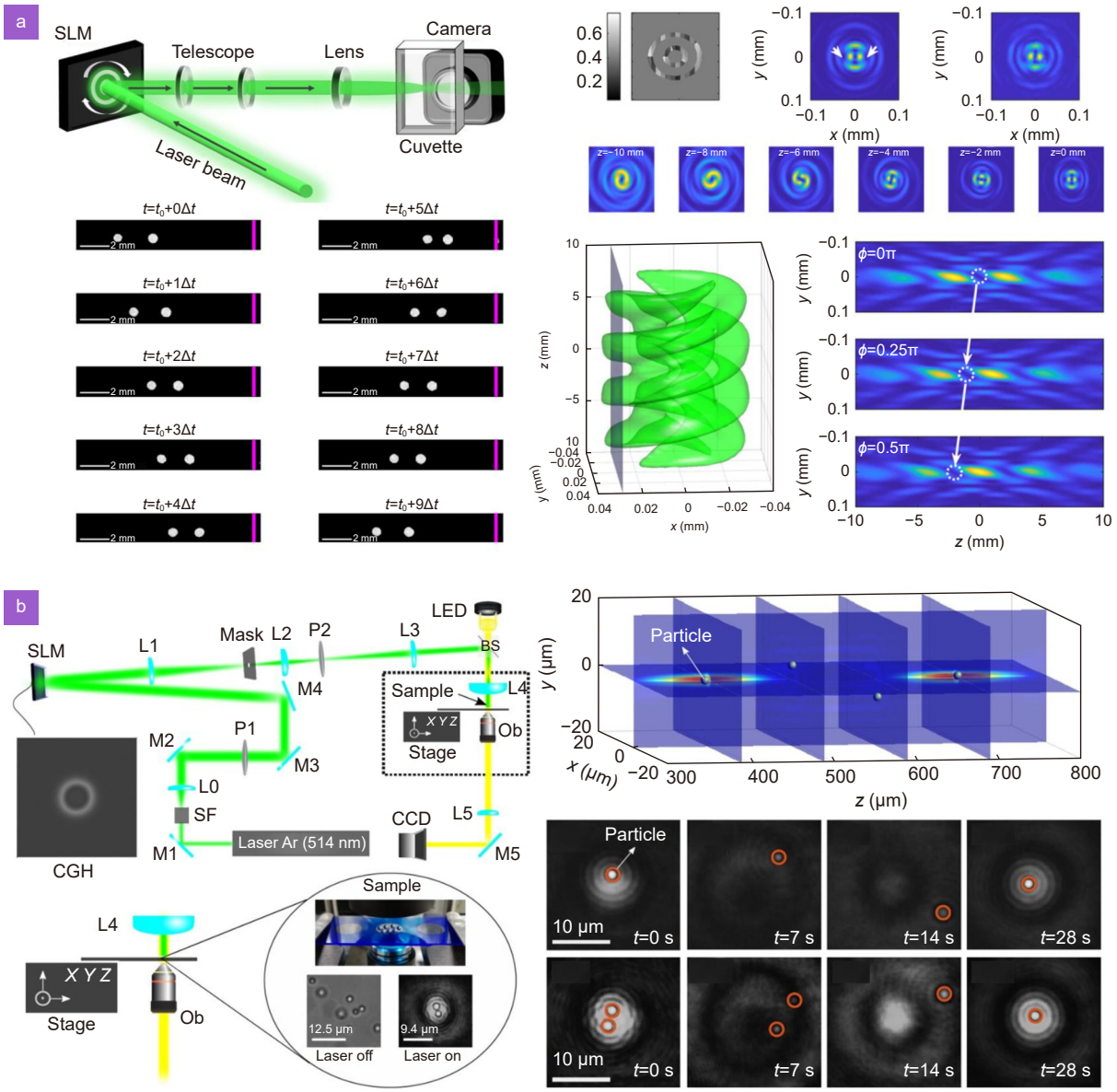

Fig. 8 | Applications of LC-SLMs in optical trapping and tweezers. (**a**) An optical analog of Archimedes' screw for particle trapping and conveying. (**b**) The first optical trapping experimental demonstration of microparticles with frozen waves. Figure reproduced from: (a) ref. [116], OSA Publishing; (b) ref. [137], OSA Publishing.

particle physics.

Measurement

Dynamic aberrations are a common problem in optical systems, and LC-SLMs offer a potential solution as an alternative to conventional deformable mirrors for aberration correction. Various high-accuracy correction systems and principles with liquid crystal wavefront correctors have been proposed[143–147]. Phase calibration has been implemented in the field of stable real-time correction[148–150] and imaging[145] with LC-SLMs. Typical applications of LC-SLMs in measurement are shown in Fig. 9. R. Li et al proposed a phase calibration technique by dividing the LC-SLM panel into two zones, the grating zone and the measured zone, enabling efficient and visible in situ calibration, as shown in Fig. 9(a)[151]. This low-cost and highly efficient method is applicable for routine and frequent calibration. A. Jesacher et al proposed a method for correcting small surface deviations of the LC-SLMs with an optical vortex and a flexible non-interferometric technique, which can be applied to optical tweezers for optimizing trapping fields and imaging systems for optimizing the point-spread-function[152]. The surface distortion information is extracted from the shape of the optical vortex. The use of LC-SLM as a phase calibration device provides a way to obtain the surface quality of

optical devices in applications, which require good characterization of amplitude, phase and polarization properties. Phase retrieval based on wavefront sensors has shown the capability of reconstructing the complex field from optical devices with high spatial resolutions. Adaptive optics (AO)[153] is one of the most promising techniques for calibrating wavefront distortions caused by atmospheric turbulence or other factors. LC-SLMs are versatile AO elements that can achieve high resolution and low temporal turbulence imaging systems for improved resolution performances and displays[154], wavefront correction for both low- and high-order aberrations in human eyes[155], etc. Combined LC-SLMs with AO techniques enable the observation of cells in their native state[156], recovery of biological or non-biological samples with near-diffraction-limited performance[157], better quality optical tweezers[158] and resolution improvements[159] in microscopy. In the context of colorful holographic images, and when dealing with broadband or incoherent light sources, the phase change of the LC-SLM at different wavelengths becomes a critical consideration. A careful calibration process is required to address the problem. This involves characterizing the phase response of the LC-SLM at different wavelengths and compensating for the wavelength-dependent phase changes. The calibration process might involve measuring the phase change introduced by the LC-SLM for various wavelengths and then applying appropriate corrections to achieve the desired holographic or wavefront manipulation. It is also possible to overcome the wavelength dependence by using a grating, but this comes at the expense of a small wavelength dependent loss factor[58].

Measurement with LC-SLM refers to the use of these devices to manipulate optical wavefronts for various purposes, which enables precise control over the characteristics of optical beams. This dynamic control enables researchers and engineers to tailor optical systems for various experimental, research, and practical purposes, ultimately enhancing the capabilities of optical technologies across diverse fields. Interferometric measurement is a powerful tool that can measure the phase profile of samples at subwavelength resolution. In the field of optical nondestructive testing, the extraction and classification of faults is a major task in industrial quality control. Interferometric fringes contain valuable information about faults in the sample, making them an important tool for defect detection. In traditional interferometry, the image-carrying light wave is coherently superposed on the reference wave, resulting in closed interference fringes that form contour lines. However, it can be challenging to distinguish between elevations and depressions using this approach. One solution to this issue is the use of a spiral phase optical element, which produces spiraled interference fringes instead of closed contour lines, enabling accurate identification of elevations and depressions[160]. The theoretical derivation of spiral interferometry and various demodulation methods based on interferograms have been extensively studied[161–163]. Researchers have also reported new quantitative phase imaging approaches based on a self-reference holograph that improves the accuracy of phase maps by superposing three on-axis interferograms with different phase filters[164]. Interferometric measurement has been successfully applied in many areas, including calculating the skew angle of a Poynting vector[165], depth measurement of polymer-coated steel samples[166], wavefront interferometry[167], detection of scattering materials[168], and measuring the optical index[169–171]. Overall, interferometric measurement is an essential tool for nondestructive testing and provides valuable information for various applications in the field of optics.

Wavefront coding

Imaging typically involves the integration of a specifically coded aperture with a coded phase mask in an optical system. One common type of device used for coded aperture imaging is the LC-SLM[172]. A diffractive lens was used in the advanced optical system of coded aperture correlation holography (COACH), which was proposed by A. Vijayakumar et al to enable 4D imaging of objects at three spatial dimensions with a spectral dimension[173]. In the same year, A. Vijayakumar et al proposed a new digital holographic imaging technique, called interferenceless coded aperture correlation holography (I-COACH), which does not rely on two-wave interference. The technique simplifies the optical systems, increases working efficiency, and eliminates complicated alignment procedures[172]. LC-SLM was employed by N. Dubey et al to generate a coded phase mask to enhance imaging resolution, as shown in Fig. 10(a)[174]. The principle of operation of endoscopic interferenceless coded aperture correlation holography (EI-COACH) is based on simulating the endoscopic setting. The annular coded phase mask is produced on the computer and displayed on the LC-SLM. The LC-SLM's internal region, surrounded by the annular coded phase mask, serves to deflect

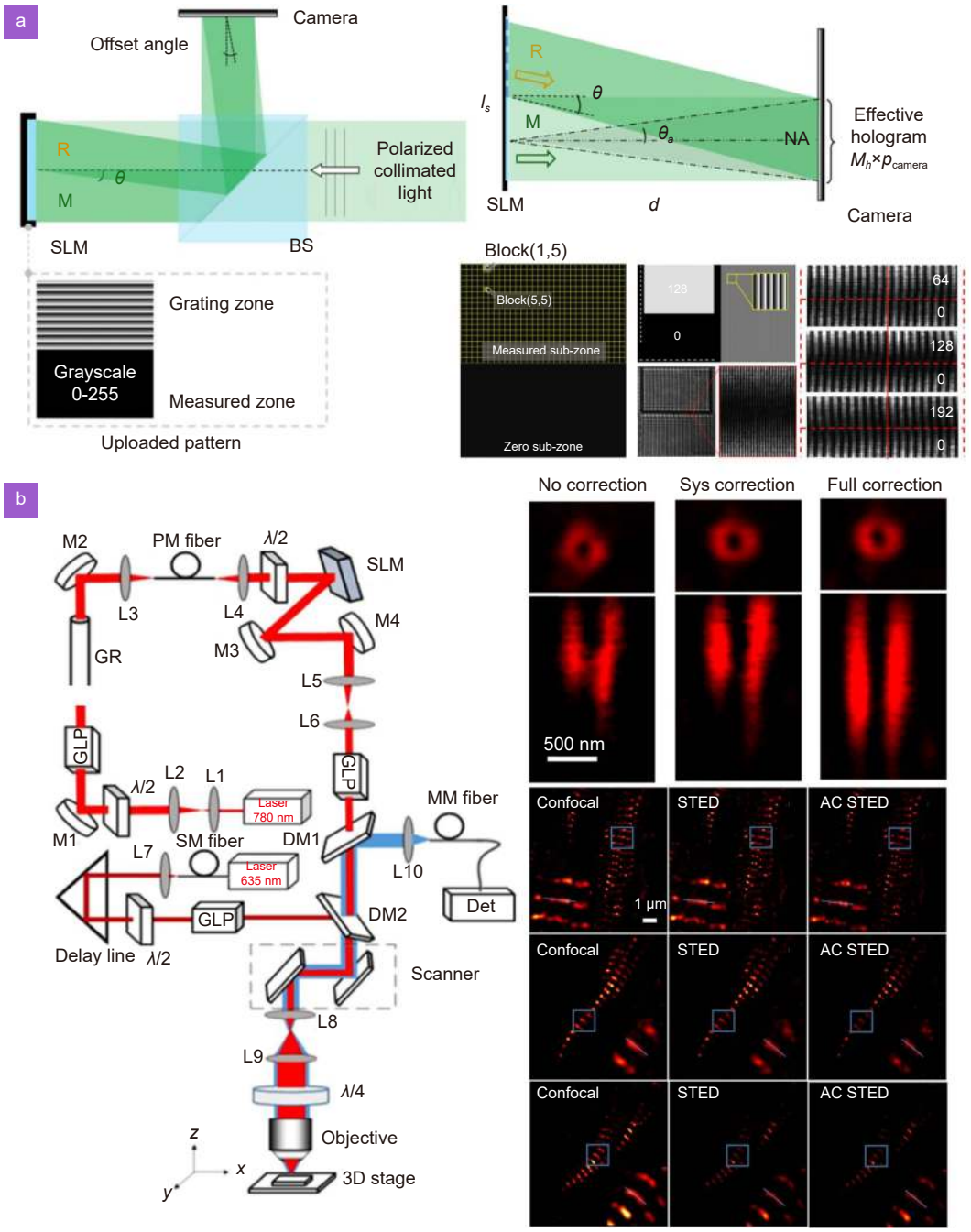

Fig. 9 | Applications of LC-SLMs in measurement. (**a**) In situ wavefront calibration based on digital holography. (**b**) Coherent optical adaptive technique can increase the spatial resolution of STED microscopy in thick samples. Figure reproduced with permission from: (a) ref.[151], SPIE; (b) ref.[159], OSA Publishing.

unwanted light through display a diffractive optical element. The diffraction optical element consists of a quadratic phase function and a linear phase function, which are used to focus unwanted light from the sensor. Thus, only the light that passes through the annular coded phase mask reaches the image sensor, and the rest dissipates around.

Random scattering of light in materials like paint, milk, and biological tissues can cause the incident wavefront to become seriously distorted, leading to a loss of spatial coherence. This results in the formation of a volume speckle field that lacks correlations over distances larger than the wavelength of light. The serious scrambling of the field makes it impossible to control the propagation of light using established wavefront calibration methods and prevents direct retrieval of the information encoded in the light. However, with active control methods, random scattering can be beneficial rather than

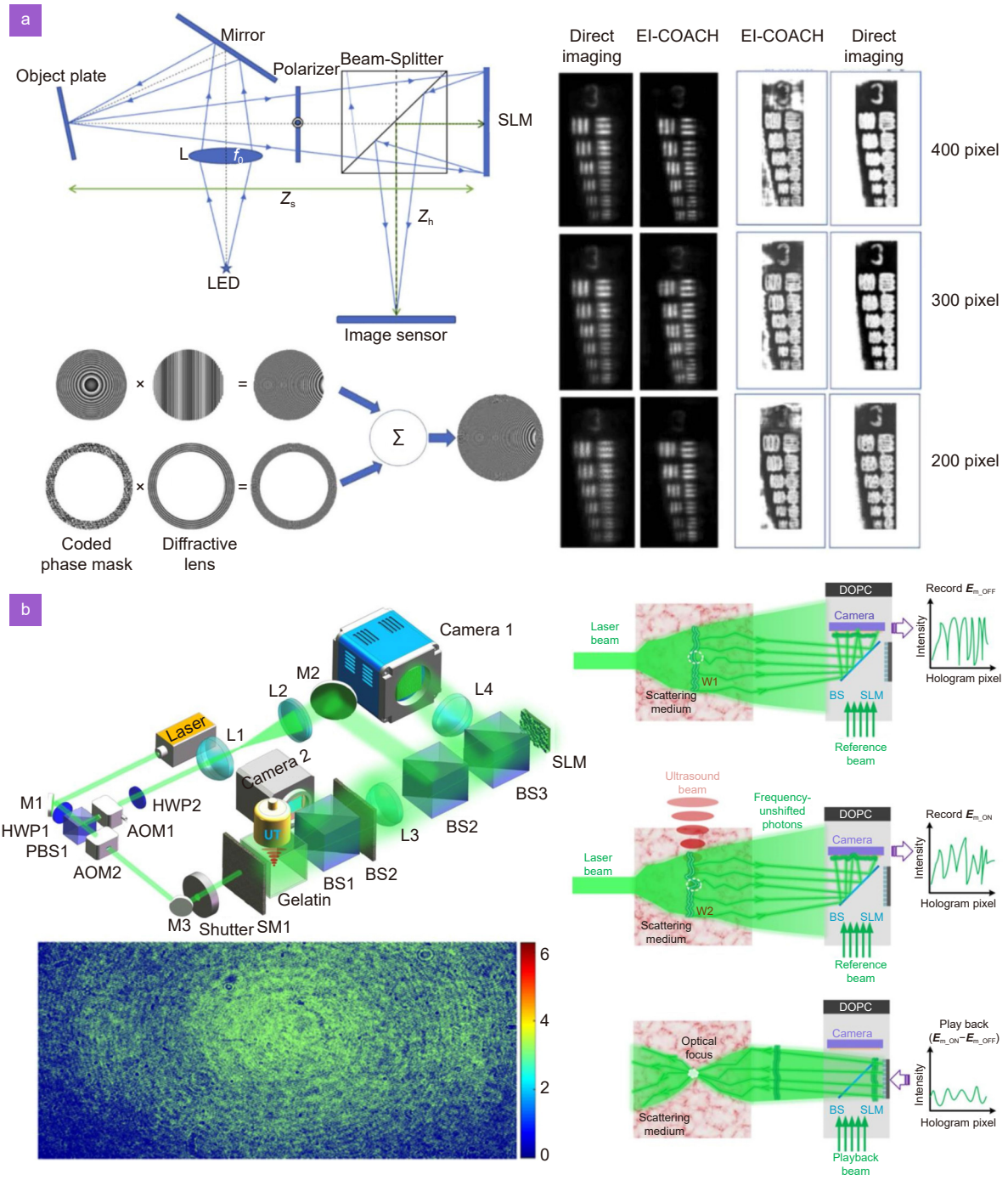

Fig. 10 | Applications of LC-SLMs in wavefront coding. (**a**) Endoscopic interferenceless coded aperture correlation holography (EI-COACH) for high-resolution coded aperture imaging. (**b**) Ultrasound-induced field perturbation (UFP) for focusing light into scattering media and speckle imaging. Figure reproduced with permission from: (a) ref.[174], OSA Publishing; (b) ref.[186], Springer Nature.

harmful for applications such as focusing[175,176], imaging[177–179], speckle analysis[180,181], phase conjugation[182–185], etc. Although challenging, effective focusing of light into or through scattering media is highly desirable in many fields. Optical scattering due to the non-uniformity of the refractive index in the scattering media makes it difficult to efficiently deliver optical intensity. Z. Cheng et al proposed a novel ultrasound-assisted technique called ultrasound-induced field perturbation optical focusing (UFP), which uses the brighter zeroth-order photons diffracted by the ultrasonic guidestar as information carriers to guide optical focusing, as shown in Fig. 10(b)[186]. The new technique allows for the focusing of light to the location where the field perturbation occurs in the

scattering medium. The technique broadens the scope of optical control in scattering media and challenges conventional notions about the usefulness of ultrasound guidestar. Biological specimens mostly consist of optical inhomogeneities, which seriously degrade imaging performances. The demand for live and real-time microscopic imaging of biological samples is high. 3D reconstruction must be fast enough to capture the dynamical properties of living cells or biological objects. True physiological imaging of subcellular dynamics requires no undue stress on the sample and characterizing the cells within their parent organisms. Therefore, wide-field in situ and native state metrology[187,188], and other biological imaging methods have been proposed[189–195].

Optical vortex

Optical vortex beams, with their unique properties, have found applications in diverse areas of research. An optical vortex beam with an $\exp(-\mathrm{i}l\phi)$ phase structure carries an orbital angular momentum of $l\hbar$ per photon, where l is the topological charge and ϕ is the azimuthal angle. When l takes on integer values, a vortex or helices is formed in the wavefront with a single screw-phase dislocation on the beam axis. When l takes on non-integer values, a complex-phase structure is formed in the wavefront, which contains many vortices at differing locations in the cross-section of the beam. When l takes on half-integer values, a line of alternating charge vortices near the radial dislocation is formed[196]. Optical vortices generically arise when laser beams are combined. A few laser beams with optical vortices can be combined to form optical vortex knots, links or loops[197,198]. LC-SLMs can efficiently synthesize the helical modes of the beam and generate novel optical vortices[199–202]. Fundamental studies on optical vortex beams include intrinsic measurement and analysis[203–214], mode generation and transformation[215–219], laser beam engineering[220–222], metrology[169], polarization nano-tomography[223], image reconstruction[224,225], and more. The OAM cannot be completely eliminated when two optical vortex beams with different topology charges are superimposed coherently. The remaining OAM in the superimposed beam, which is located in different concentric circles, may have the opposite orientation due to the difference in charge. When the different charges of the two beams are large, the remaining OAM can be detected through the rotating micro-particles[226,227].

Optical vortex has been widely used in optical communication due to its capability of providing more degrees of freedom and expanding the bandwidth[228–233]. Typical applications of LC-SLMs in optical vortex are shown in Fig. 11. M. Malik et al proposed an OAM modal for a free-space 11-dimensional communication system[232]. By combining LC-SLM with binary phase filters, the transmission bandwidth of multimode fibers can be largely increased. G. Jing et al proposed a fractional orbital angular momentum (FOAM) mode recognition method with a feedforward neural network (FNN)[234]. The experiment result showed that the method can break the limitation of precision measurement in the turbulence environment of practical FOAM applications. To further increase the data transmission rate, in addition to OAM, A. Trichili et al demonstrated the use of both radial and azimuthal degrees of freedom for multiplexing and demultiplexing, as shown in Fig. 11(b)[235]. The novel holographic technique allowed over 100 modes to be encoded and decoded in one hologram, in a wide wavelength range through a wavelength-independent manner. Optical vortex beams offer immense potential for developing innovative optical communication techniques and are an active area of research.

Quantum applications

Quantum optics has traditionally been executed experimentally using qubit quantum states based on polarization, for which the optical toolkit is very mature. The birth of spatial modes of light as a basis to realize high-dimensional quantum states has opened up many new quantum processes and protocols[236,237], all facilitated by LC-SLMs embedded as quantum state creators and detectors, as shown in Fig. 12(a). The birth of this field can be traced back to the seminal work in 2001 where DOEs were used as OAM projectors to show OAM conservation down to the single photon level, and OAM entanglement in 2D subspaces[238]. The DOEs, which were hard-coded for particular projections, were later replaced by LC-SLMs for rewritable quantum projectors, one for each photon in the experiment. This was a crucial step, particularly when considering that there are many spatial basis to select from, and an infinite number of modes in each. This implies the need to have versatility in the detection step, a condition made possible with SLMs. For instance, the introduction of LC-SLMs into quantum optics enabled dynamic quantum state tomography, first for OAM qubits[239] and later for any dimensional state on any basis[240]. This was quickly followed by seminal work

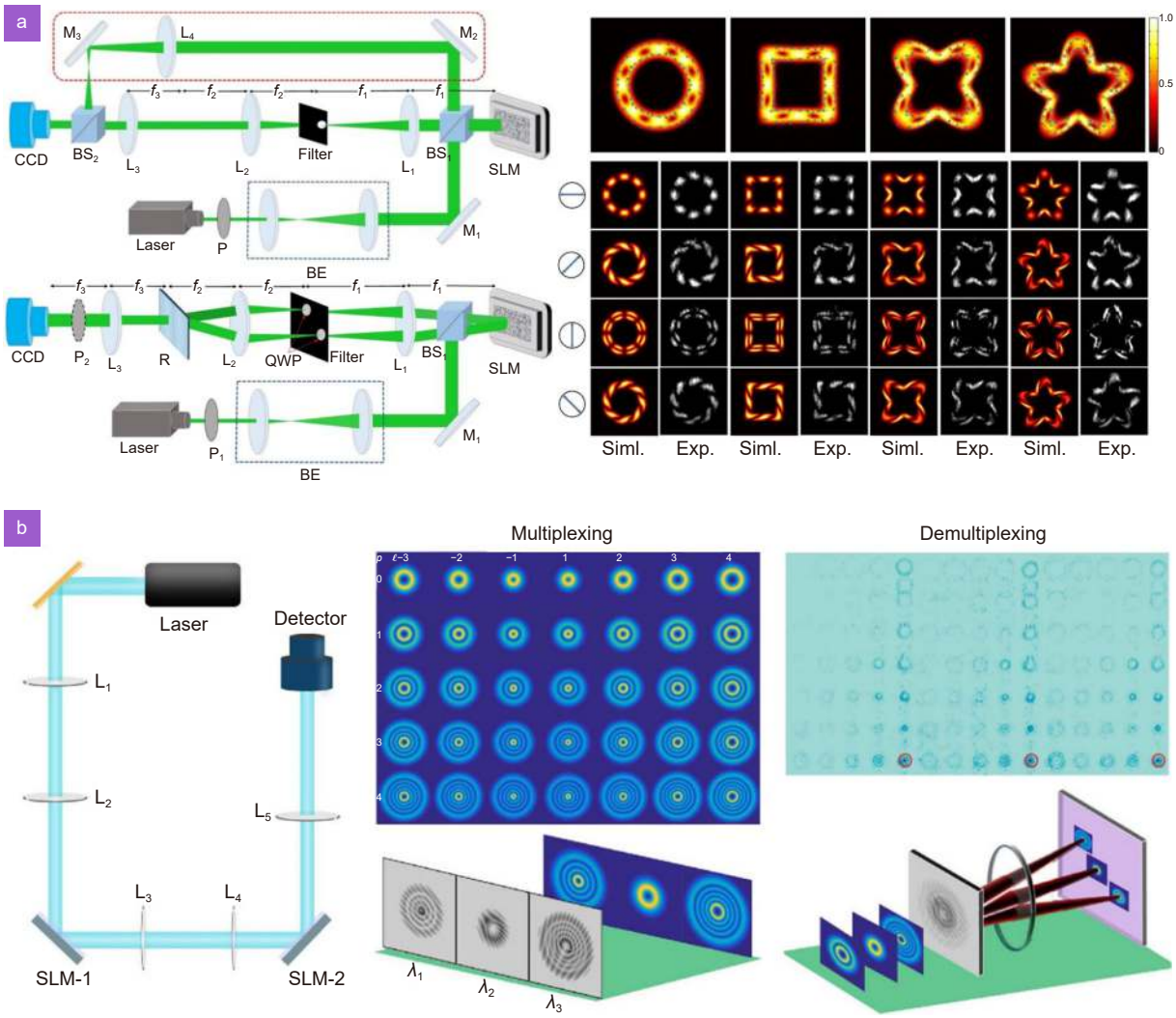

Fig. 11 | Applications of LC-SLMs in optical vortex. (**a**) Optical vortex array generation aligned along an arbitrary curvilinear path. (**b**) Optical communication beyond orbital angular momentum can generate over 100 channels with one hologram. Figure reproduced with permission from: (a) ref.[216], OSA Publishing; (b) ref.[235], Springer Nature.

on Bell inequality violations using digital holograms[241], uncertainty principle tests[242] and the realization of ultra-high entangled state characterization using just a few measurements[243,244]. LC-SLMs have likewise proven essential in tailoring the entanglement spectrum either at the creation step[245–247] or the detection step[248,249]. This realization and control of multidimensional quantum states have led to both new physics and advanced quantum applications, with LC-SLMs proving crucial in quantum random number generation[250], quantum key distribution[251,252], quantum communication[253,254], quantum secret sharing[255] and for quantum entanglement swapping[256] and teleportation[257], reaching states of up to 100 × 100 dimensions[258]. Figure 12 illustrates the typical applications of LC-SLMs in the field of quantum. The quantum application that is most leveraged in the use of SLMs is quantum ghost imaging[259–262], where digital objects are encoded on one photon and digitally detected on the other photon. Here the SLMs facilitate computational approaches to be used, for instance, to allow single pixel imaging with random masks on the SLMs.

Summary and outlook

LC-SLMs have had a profound impact on various research areas and applications, ranging from optical interconnections at the component level to quantum entanglement. This review paper provides a comprehensive analysis of recent developments in LC-SLMs by discussing liquid crystal devices, exploring light shaping through diffraction, and highlighting the promising applications of LC-SLMs. The review demonstrates the po-

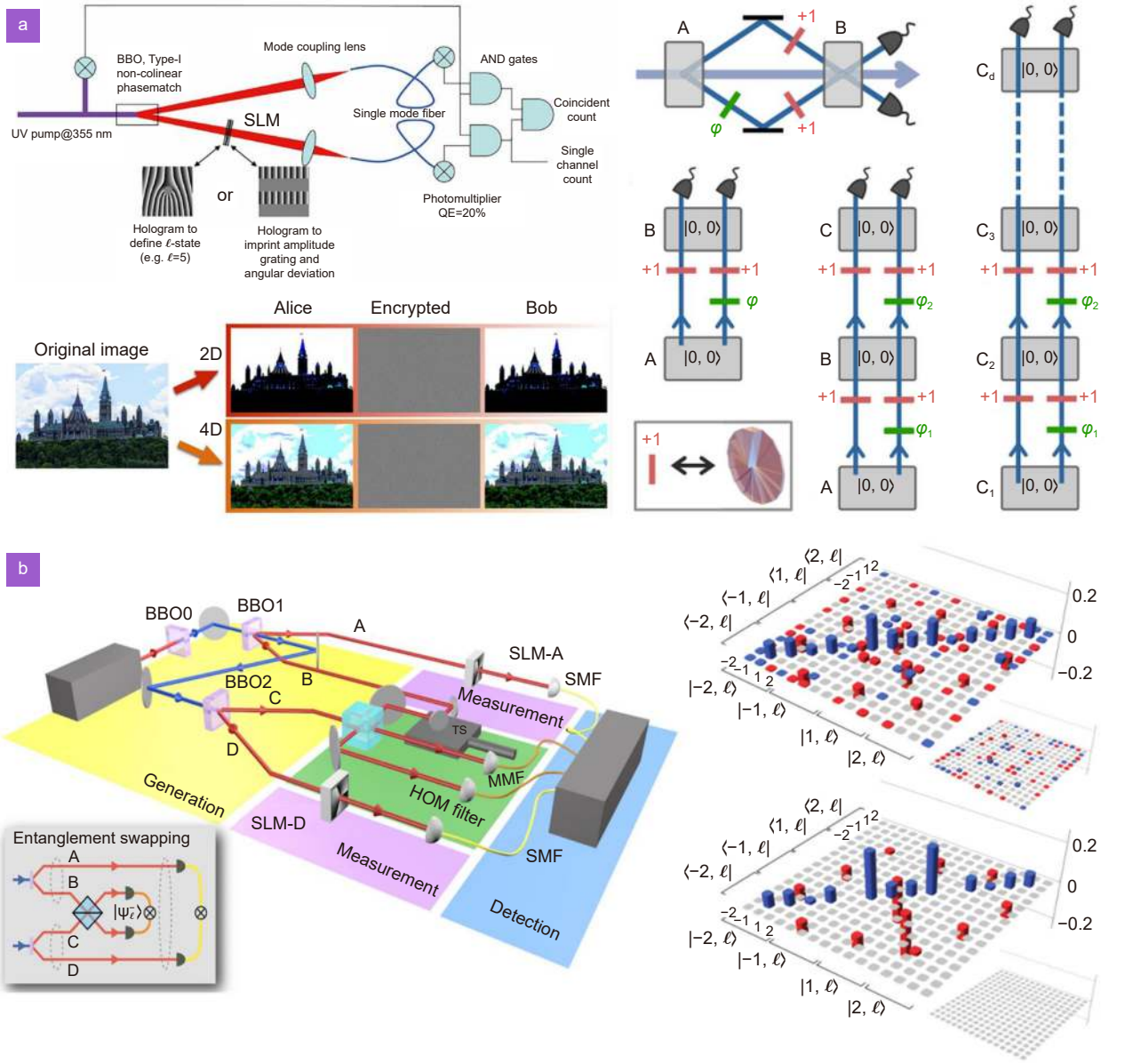

Fig. 12 | Applications of LC-SLMs in quantum applications. (**a**) High dimensional and multidimensional entanglement with structured light. (**b**) Quantum entanglement swapping of multiple orbital angular momentum states of light simultaneously. Figure reproduced with permission from: (a) ref.[237], AIP Publishing LLC; (b) ref.[256], Springer Nature.

tential of LC-SLMs to achieve unique functionalities, but also outlines the technical challenges that need to be addressed to advance this field further. One significant challenge is the lack of compact and fast enough LC-SLMs, especially in long-wave wavelengths. Additionally, designing LC-SLM systems involve trade-offs among various factors, such as resolution, modulation range, and damage threshold. Reducing pixel size and increasing the number of pixels in an image can improve image clarity and quality, but may also compromise fill factor, surface flatness, diffraction efficiency, and light utilization. Presently, the maximum matrix resolution is 4160×2464 and a linear array of 1×12288. Several methods have been proposed to achieve large-angle holographic displays, but there is a trade-off between modulation range and refresh rate. Furthermore, the high concentration of laser energy can cause deformation or complete damage to the inside or surface of the medium. This damage is related to the processing of optical components, such as the coating methods and the purity of the film material. Short response time is crucial in applications that require real-time modulation of optical wavefronts. This is particularly important in dynamic applications. Long response time can limit the ability of

LC-SLMs to keep up with rapidly changing optical signals, leading to degraded performance and reduced effectiveness. Overcoming this challenge requires the development of LC-SLMs technologies that can swiftly modulate phase and amplitude while maintaining accuracy. High resolution refers to the number of pixels per unit area on the LC-SLM. For precise modulation of optical wavefronts, a high resolution is crucial. However, increasing the pixel density presents challenges related to manufacturing, controlling individual pixels, and managing heat dissipation. Higher resolution demands better control over individual pixels, which can lead to difficulties in maintaining uniformity and minimizing cross-talk between adjacent pixels. Advanced manufacturing techniques, pixel addressing schemes, and materials engineering are being explored to pursue higher resolution without compromising performance. Fringe field effects occur due to interactions between pixels on an LC-SLM, resulting in unintended phase or amplitude changes in neighboring pixels. These effects can lead to image artifacts, reduced modulation fidelity, and inaccurate wavefront manipulation. Mitigating these effects requires precise pixel addressing and calibration techniques, as well as the development of pixel structures that minimize cross-talk. As these challenges are overcome, LC-SLMs are becoming more versatile tools for dynamic optical control, holography, imaging, and many other fields where precise wavefront manipulation is essential.

We conclude by providing our opinions on the opportunities and technical challenges in the rapidly developing field of metamaterials and metasurfaces. Metamaterials have been a research hotspot and offer the ability to modulate various properties of light such as bandwidth, polarization, wavelength, and time dependence. By incorporating metamaterials into LC-SLMs, a substitute optical modality is possible. Ongoing research in this realm aims to improve the usefulness of long-wave metamaterial imaging, which has significant implications for non-invasive cancer detection, infrared thermography, and other medical imaging scenarios. Another promising direction is the use of metasurfaces, which can perform wavefront regulation at the sub-wavelength scale. Metasurfaces can be implemented in designing and fabricating optical elements and systems with capabilities that surpass the performance of conventional DOEs. By integrating metasurfaces with LC-SLMs, one can make LC-SLMs more powerful in wavefront engineering, modulation of polarized light, holography, and other applications. S. Mansha et al proposed a novel design that allows small pixel and multi-spectral operations with a metasurface-based LC-SLM[263]. Their design is based on LC-tunable Fabry-Perot nanocavities, which are designed to support multiple resonances in the visible range, including RGB wavelengths, providing continuous 2π phase modulation with high reflectance. It is foreseeable that with the improvements in manufacturing techniques, computing power and further exploration of dynamic modulation techniques, the performance of LC-SLMs could be further improved. The incorporation of metamaterials and metasurfaces into LC-SLMs opens up new exciting possibilities for research and applications in various fields. However, there are still technical challenges that need to be addressed, such as improving the usefulness of long-wave metamaterial techniques, optimizing the design and fabrication of metasurface-based LC-SLMs. Nonetheless, we are optimistic about the future of LC-SLMs and the potential impact they can have on the field of optics and beyond.

References

1. Forbes A, de Oliveira M, Dennis MR. Structured light. *Nat Photonics* **15**, 253–262 (2021).
2. He C, Shen YJ, Forbes A. Towards higher-dimensional structured light. *Light Sci Appl* **11**, 205 (2022).
3. Buono WT, Forbes A. Nonlinear optics with structured light. *Opto-Electron Adv* **5**, 210174 (2022).
4. Dickey FM, Lizotte TE. *Laser Beam Shaping Applications* (CRC Press, Boca Raton, 2006).
5. Dickey FM. *Laser Beam Shaping*: *Theory and Techniques* 2nd ed (CRC Press, Boca Raton, 2014).
6. Dickey FM. Laser beam shaping. *Opt Photonics News* **14**, 30–35 (2003).
7. Rhodes PW, Shealy DL. Refractive optical systems for irradiance redistribution of collimated radiation: their design and analysis. *Appl Opti* **19**, 3545–3553 (1980).
8. Lohmann AW. A pre-history of computer-generated holography. *Opt Photonics News* **19**, 36–47 (2008).
9. Soifer AV, Kotlar V, Doskolovich L. *Iteractive Methods for Diffractive Optical Elements Computation* (London, CRC Press, 1997).
10. Soifer VA, Golub MA. *Laser Beam Mode Selection by Computer Generated Holograms* (Boca Raton, CRC Press, 1994).
11. Soifer VA. *Methods for Computer Design of Diffractive Optical Elements* (Willey, New York, 2002).
12. Soifer VA. *Diffractive Optics and Nanophotonics* (CRC Press, Boca Raton, 2017).
13. Lazarev G, Chen PJ, Strauss J, Fontaine N, Forbes A. Beyond the display: phase-only liquid crystal on silicon devices and their applications in photonics [Invited]. *Opt Express* **27**, 16206–16249 (2019).
14. Zhang ZC, You Z, Chu DP. Fundamentals of phase-only liquid crystal on silicon (LCOS) devices. *Light Sci Appl* **3**, e213

(2014).
15. Huang YG, Liao E, Chen R, Wu ST. Liquid-crystal-on-silicon for augmented reality displays. *Appl Sci* **8**, 2366 (2018).
16. Xiong JH, Wu ST. Planar liquid crystal polarization optics for augmented reality and virtual reality: from fundamentals to applications. *eLight* **1**, 3 (2021).
17. Lu YQ, Li Y. Planar liquid crystal polarization optics for near-eye displays. *Light Sci Appl* **10**, 122 (2021).
18. Berto P, Philippet L, Osmond J, Liu CF, Afridi A et al. Tunable and free-form planar optics. *Nat Photonics* **13**, 649–656 (2019).
19. Sui XM, He ZH, Cao LC, Jin GF. Recent progress in complex-modulated holographic display based on liquid crystal spatial light modulators. *Chin J Liq Cryst Dis* **36**, 797–809 (2021).
20. Li RJ, Cao LC. Progress in phase calibration for liquid crystal spatial light modulators. *Appl Sci* **9**, 2012 (2019).
21. Rosales-Guzmán C, Forbes A. *How to Shape Light with Spatial Light Modulators* (SPIE, 2017).
22. Forbes A, Dudley A, McLaren M. Creation and detection of optical modes with spatial light modulators. *Adv Opt Photonics* **8**, 200–227 (2016).
23. Weiner AM. Femtosecond pulse shaping using spatial light modulators. *Rev Sci Instrum* **71**, 1929–1960 (2000).
24. Weiner AM. Ultrafast optical pulse shaping: a tutorial review. *Opt Commun* **284**, 3669–3692 (2011).
25. Szuniewicz J, Kurdziałek S, Kundu S, Zwolinski W, Chrapkiewicz R et al. Noise-resistant phase imaging with intensity correlation. *Science Advances* **9**, eadh5396 (2023).
26. Yao E, Franke-Arnold S, Courtial J, Padgett MJ, Barnett SM. Observation of quantum entanglement using spatial light modulators. *Opt Express* **14**, 13089–13094 (2006).
27. Kong LJ, Sun YF, Zhang FR, Zhang JF, Zhang XD. High-dimensional entanglement-enabled holography. *Physical Review Letters* **130**, 053602 (2023).
28. Maurer C, Jesacher A, Bernet S, Ritsch-Marte M. What spatial light modulators can do for optical microscopy. *Laser Photonics Rev* **5**, 81–101 (2011).
29. Shapiro JH. Computational ghost imaging. *Phys Rev A* **78**, 061802 (2008).
30. Moreau PA, Toninelli E, Gregory T, Padgett MJ. Ghost imaging using optical correlations. *Laser Photonics Rev* **12**, 1700143 (2018).
31. Padgett M, Bowman R. Tweezers with a twist. *Nat Photonics* **5**, 343–348 (2011).
32. Grier DG. A revolution in optical manipulation. *Nature* **424**, 810–816 (2003).
33. Sun BS, Salter PS, Roider C, Jesacher A, Strauss J et al. Four-dimensional light shaping: manipulating ultrafast spatiotemporal foci in space and time. *Light Sci Appl* **7**, 17117 (2018).
34. Jesacher A, Maurer C, Schwaighofer A, Bernet S, Ritsch-Marte M. Near-perfect hologram reconstruction with a spatial light modulator. *Opt Express* **16**, 2597–2603 (2008).
35. Meng XS, Qiu XY, Li GQ, Ye WJ, Lin YQ et al. Study of optical rotation generated by the twisted nematic liquid crystal film: based on circular birefringence effect. *Appl Opt* **58**, 5301–5309 (2019).
36. Hua H, Liu Y, Yong K. The effect of pretilt and twisted angle on twisted nematic liquid crystal filter. *Opt Spectrosc* **125**, 275–280 (2018).
37. Lagerwall JPF, Scalia G. A new era for liquid crystal research: applications of liquid crystals in soft matter nano-, bio- and microtechnology. *Curr Appl Phys* **12**, 1387–1412 (2012).
38. Efron U, Wu ST, Bates TD. Nematic liquid crystals for spatial light modulators: recent studies. *J Opt Soc Am B* **3**, 247–252 (1986).
39. Konforti N, Marom E, Wu ST. Phase-only modulation with twisted nematic liquid-crystal spatial light modulators. *Opt Lett* **13**, 251–253 (1988).
40. Wen L, Nan XH, Li JX, Cumming DRS, Hu X et al. Broad-band spatial light modulation with dual epsilon-near-zero modes. *Opto-Electron Adv* **5**, 200093 (2022).
41. Tang DL, Shao ZL, Xie X, Zhou YJ, Zhang XH et al. Flat multifunctional liquid crystal elements through multi-dimensional information multiplexing. *Opto-Electron Adv* **6**, 220063 (2023).
42. Chen HMP, Yang JP, Yen HT, Hsu ZN, Huang YG et al. Pursuing high quality phase-only liquid crystal on silicon (LCoS) devices. *Appl Sci* **8**, 2323 (2018).
43. Tabiryan NV, Roberts DE, Liao Z, Hwang JY, Moran M et al. Advances in transparent planar optics: enabling large aperture, ultrathin lenses. *Adv Opt Mater* **9**, 2001692 (2021).
44. Wen YF, Zhang Q, He Q, Zhang FF, Xiong LX et al. Shortening focal length of 100-mm aperture flat lens based on improved sagnac interferometer and bifacial liquid crystal. *Adv Opt Mater* **11**, 2300127 (2023).
45. Nassiri MG, Brasselet E. Multispectral management of the photon orbital angular momentum. *Phys Rev Lett* **121**, 213901 (2018).
46. Brasselet E. Tunable high-resolution macroscopic self-engineered geometric phase optical elements. *Phys Rev Lett* **121**, 033901 (2018).
47. McGloin D, Dholakia K. Bessel beams: diffraction in a new light. *Contemp Phys* **46**, 15–28 (2005).
48. Siviloglou GA, Broky J, Dogariu A, Christodoulides DN. Observation of accelerating Airy beams. *Phys Rev Lett* **99**, 213901 (2007).
49. Carter WH. Spot size and divergence for Hermite Gaussian beams of any order. *Appl Opt* **19**, 1027–1029 (1980).
50. Zauderer E. Complex argument Hermite–Gaussian and Laguerre–Gaussian beams. *J Opt Soc Am A* **3**, 465–469 (1986).
51. Allen L, Beijersbergen MW, Spreeuw RJC, Woerdman JP. Orbital angular momentum of light and the transformation of Laguerre-Gaussian laser modes. *Phys Rev A* **45**, 8185–8189 (1992).
52. Yang YQ, Kang XW, Cao LC. Robust propagation of a steady optical beam through turbulence with extended depth of focus based on spatial light modulator. *J Phys Photonics* **5**, 035002 (2023).
53. Göröcs Z, Erdei G, Sarkadi T, Ujhelyi F, Reményi J et al. Hybrid multinary modulation using a phase modulating spatial light modulator and a low-pass spatial filter. *Opt Lett* **32**, 2336–2338 (2007).
54. Frumker E, Silberberg Y. Phase and amplitude pulse shaping with two-dimensional phase-only spatial light modulators. *J Opt Soc Am B* **24**, 2940–2947 (2007).
55. Supradeepa VR, Huang CB, Leaird DE, Weiner AM. Femtosecond pulse shaping in two dimensions: towards higher complexity optical waveforms. *Opt Express* **16**, 11878–11887 (2008).

56. Paurisse M, Hanna M, Druon F, Georges P, Bellanger C et al. Phase and amplitude control of a multimode LMA fiber beam by use of digital holography. *Opt Express* **17**, 13000–13008 (2009).
57. Karimi E, Zito G, Piccirillo B, Marrucci L, Santamato E. Hypergeometric-Gaussian modes. *Opt Lett* **32**, 3053–3055 (2007).
58. Spangenberg DM, Dudley A, Neethling PH, Rohwer EG, Forbes A. White light wavefront control with a spatial light modulator. *Opt Express* **22**, 13870–13879 (2014).
59. Zacharias T, Hadad B, Bahabad A, Eliezer Y. Axial sub-Fourier focusing of an optical beam. *Opt Lett* **42**, 3205–3208 (2017).
60. Zhu LW, Yang R, Zhang DW, Yu JJ, Chen JN. Dynamic three-dimensional multifocal spots in high numerical-aperture objectives. *Opt Express* **25**, 24756–24766 (2017).
61. Zeng TT, Chang CL, Chen ZZ, Wang HY, Ding JP. Three-dimensional vectorial multifocal arrays created by pseudo-period encoding. *J Opt* **20**, 065605 (2018).
62. Vellekoop IM, van Putten EG, Lagendijk A, Mosk AP. Demixing light paths inside disordered metamaterials. *Opt Express* **16**, 67–80 (2008).
63. Vellekoop IM, Mosk AP. Universal optimal transmission of light through disordered materials. *Phys Rev Lett* **101**, 120601 (2008).
64. Hsieh CL, Pu Y, Grange R, Psaltis D. Digital phase conjugation of second harmonic radiation emitted by nanoparticles in turbid media. *Opt Express* **18**, 12283–12290 (2010).
65. Popoff SM, Lerosey G, Carminati R, Fink M, Boccara AC et al. Measuring the transmission matrix in optics: an approach to the study and control of light propagation in disordered media. *Phys Rev Lett* **104**, 100601 (2010).
66. Popoff S, Lerosey G, Fink M, Boccara AC, Gigan S. Image transmission through an opaque material. *Nat Commun* **1**, 81 (2010).
67. Mazilu M, Baumgartl J, Kosmeier S, Dholakia K. Optical eigenmodes; exploiting the quadratic nature of the energy flux and of scattering interactions. *Opt Express* **19**, 933–945 (2011).
68. Madan I, Leccese V, Mazur A, Barantani F, LaGrange T et al. Ultrafast transverse modulation of free electrons by interaction with shaped optical fields. *ACS Photonics* **9**, 3215–3224 (2022).
69. Fu SY, Zhang SK, Gao CQ. Bessel beams with spatial oscillating polarization. *Sci Rep* **6**, 30765 (2016).
70. Fu SY, Wang TL, Zhang ZY, Zhai YW, Gao CQ. Non-diffractive Bessel-Gauss beams for the detection of rotating object free of obstructions. *Opt Express* **25**, 20098–20108 (2017).
71. Wang F, Li J, Martinez-Piedra G, Korotkova O. Propagation dynamics of partially coherent crescent-like optical beams in free space and turbulent atmosphere. *Opt Express* **25**, 26055–26066 (2017).
72. Zhu GX, Wen YH, Wu X, Chen YJ, Liu J et al. Obstacle evasion in free-space optical communications utilizing Airy beams. *Opt Lett* **43**, 1203–1206 (2018).
73. Lin H, Jia BH, Gu M. Dynamic generation of Debye diffraction-limited multifocal arrays for direct laser printing nanofabrication. *Opt Lett* **36**, 406–408 (2011).
74. Lightman S, Hurvitz G, Gvishi R, Arie A. Miniature wide-spectrum mode sorter for vortex beams produced by 3D laser printing. *Optica* **4**, 605–610 (2017).
75. Okada T, Tanaka K. Photo-designed terahertz devices. *Sci Rep* **1**, 121 (2011).
76. Trichili A, Mhlanga T, Ismail Y, Roux FS, McLaren M et al. Detection of Bessel beams with digital axicons. *Opt Express* **22**, 7553–17560 (2014).
77. Jenness NJ, Wu YQ, Clark RL. Fabrication of three-dimensional electrospun microstructures using phase modulated femtosecond laser pulses. *Mater Lett* **66**, 360–363 (2012).
78. Yang L, Ji SY, Xie KA, Du WQ, Liu BJ et al. High efficiency fabrication of complex microtube arrays by scanning focused femtosecond laser Bessel beam for trapping/releasing biological cells. *Opt Express* **25**, 8144–8157 (2017).
79. Sun XY, Dong ZL, Cheng KF, Chu DK, Kong DJ et al. Fabrication of oil–water separation copper filter by spatial light modulated femtosecond laser. *J Micromech Microeng* **30**, 065007 (2020).
80. Pan D, Xu B, Liu SL, Li JW, Hu YL et al. Amplitude-phase optimized long depth of focus femtosecond axilens beam for single-exposure fabrication of high-aspect-ratio microstructures. *Opt Lett* **45**, 2584–2587 (2020).
81. Xavier J, Boguslawski M, Rose P, Joseph J, Denz C. Reconfigurable optically induced quasicrystallographic three-dimensional complex nonlinear photonic lattice structures. *Adv Mater* **22**, 356–360 (2010).
82. Yuan YJ, Jiang L, Li X, Zuo P, Xu CY et al. Laser photonic-reduction stamping for graphene-based micro-supercapacitors ultrafast fabrication. *Nat Commun* **11**, 6185 (2020).
83. Kelner R, Rosen J. Methods of single-channel digital holography for three-dimensional imaging. *IEEE Trans Ind Inf* **12**, 220–230 (2016).
84. Reicherter M, Zwick S, Haist T, Kohler C, Tiziani H et al. Fast digital hologram generation and adaptive force measurement in liquid-crystal-display-based holographic tweezers. *Appl Opt* **45**, 888–896 (2006).
85. Euser TG, Whyte G, Scharrer M, Chen JSY, Abdolvand A et al. Dynamic control of higher-order modes in hollow-core photonic crystal fibers. *Opt Express* **16**, 17972–17981 (2008).
86. Katz B, Wulich D, Rosen J. Optimal noise suppression in Fresnel incoherent correlation holography (FINCH) configured for maximum imaging resolution. *Appl Opt* **49**, 5757–5763 (2010).
87. Shimobaba T, Kakue T, Yamamoto Y, Hoshi I, Shiomi H et al. Hologram generation via Hilbert transform. *OSA Continuum* **3**, 1498–1503 (2020).
88. Zhao Y, Cao LC, Zhang H, Kong DZ, Jin GF. Accurate calculation of computer-generated holograms using angular-spectrum layer-oriented method. *Opt Express* **23**, 25440–25449 (2015).
89. Shi L, Li BC, Kim C, Kellnhofer P, Matusik W. Towards real-time photorealistic 3D holography with deep neural networks. *Nature* **591**, 234–239 (2021).
90. Sui XM, He ZH, Zhang H, Cao LC, Jin GF. Spatiotemporal double-phase hologram for complex-amplitude holographic displays. *Chin Opt Lett* **18**, 100901 (2020).
91. Christenson CW, Blanche PA, Tay S, Voorakaranam R, Gu T et al. Materials for an updatable holographic 3D display. *J Disp Technol* **6**, 510–516 (2010).
92. Kim J, Gopakumar M, Choi S, Peng YF, Lopes W et al. Holographic glasses for virtual reality. In *Proceedings of ACM SIGGRAPH 2022 Conference Proceedings* 33 (ACM, 2022);https://doi.org/10.1145/3528233.3530739.
93. Sato H, Kakue T, Ichihashi Y, Endo Y, Wakunami K et al. Real-time colour hologram generation based on ray-sampling

plane with multi-GPU acceleration. *Sci Rep* **8**, 1500 (2018).
94. Cao HK, Lin SF, Kim ES. Accelerated generation of holographic videos of 3-D objects in rotational motion using a curved hologram-based rotational-motion compensation method. *Opt Express* **26**, 21279–21300 (2018).
95. Derzhypolskyi AG, Gnatovskyi OV, Derzhypolska LA. Reduction of speckle noise in laser energy distribution on the target by means of modified fourier hologram and incoherent averaging technique. *Semicond Phys Quantum Electron Optoelectron* **21**, 429–433 (2018).
96. Choi S, Gopakumar M, Peng YF, Kim J, O'Toole M et al. Time-multiplexed neural holography: a flexible framework for holographic near-eye displays with fast heavily-quantized spatial light modulators. In *Proceedings of ACM SIGGRAPH 2022 Conference Proceedings* 32 (ACM, 2022); https://doi.org/10.1145/3528233.3530734.
97. Lee JS, Kim YK, Won YH. Time multiplexing technique of holographic view and Maxwellian view using a liquid lens in the optical see-through head mounted display. *Opt Express* **26**, 2149–2159 (2018).
98. Tsutsumi N, Kinashi K, Sakai W, Nishide J, Kawabe Y et al. Real-time three-dimensional holographic display using a monolithic organic compound dispersed film. *Opt Mater Express* **2**, 1003–1010 (2012).
99. Yeom HJ, Kim HJ, Kim SB, Zhang HJ, Li BN et al. 3D holographic head mounted display using holographic optical elements with astigmatism aberration compensation. *Opt Express* **23**, 32025–32034 (2015).
100. Choi MH, Ju YG, Park JH. Holographic near-eye display with continuously expanded eyebox using two-dimensional replication and angular spectrum wrapping. *Opt Express* **28**, 533–547 (2020).
101. Rostykus M, Moser C. Compact lensless off-axis transmission digital holographic microscope. *Opt Express* **25**, 16652–16659 (2017).
102. Kim D, Nam SW, Lee B, Seo JM, Lee B. Accommodative holography: improving accommodation response for perceptually realistic holographic displays. *ACM Trans Graph* **41**, 111 (2022).
103. Zhou PC, Li Y, Liu SX, Su YK. Compact design for optical-see-through holographic displays employing holographic optical elements. *Opt Express* **26**, 22866–22876 (2018).
104. Park JH, Kim SB. Optical see-through holographic near-eye-display with eyebox steering and depth of field control. *Opt Express* **26**, 27076–27088 (2018).
105. Chang CL, Qi YJ, Wu J, Xia J, Nie SP. Speckle reduced lensless holographic projection from phase-only computer-generated hologram. *Opt Express* **25**, 6568–6580 (2017).
106. Maimone A, Georgiou A, Kollin JS. Holographic near-eye displays for virtual and augmented reality. *ACM Trans Graph* **36**, 85 (2017).
107. Shi L, Huang FC, Lopes W, Matusik W, Luebke D. Near-eye light field holographic rendering with spherical waves for wide field of view interactive 3D computer graphics. *ACM Trans Graph* **36**, 236 (2017).
108. Yamada S, Kakue T, Shimobaba T, Ito T. Interactive holographic display based on finger gestures. *Sci Rep* **8**, 2010 (2018).
109. Jordan P, Leach J, Padgett M, Blackburn P, Isaacs N et al. Creating permanent 3D arrangements of isolated cells using holographic optical tweezers. *Lab Chip* **5**, 1224–1228 (2005).
110. Burnham DR, McGloin D. Holographic optical trapping of aerosol droplets. *Opt Express* **14**, 4175–4181 (2006).
111. Chapin SC, Germain V, Dufresne ER. Automated trapping, assembly, and sorting with holographic optical tweezers. *Opt Express* **14**, 13095–13100 (2006).
112. He XD, Xu P, Wang J, Zhan MS. Rotating single atoms in a ring lattice generated by a spatial light modulator. *Opt Express* **17**, 21007–21014 (2009).
113. Hörner F, Woerdemann M, Müller S, Maier B, Denz C. Full 3D translational and rotational optical control of multiple rod-shaped bacteria. *J Biophoton* **3**, 468–475 (2010).
114. Thalhammer G, Steiger R, Bernet S, Ritsch-Marte M. Optical macro-tweezers: trapping of highly motile micro-organisms. *J Opt* **13**, 044024 (2011).
115. Liang YS, Lei M, Yan SH, Li MM, Cai YA et al. Rotating of low-refractive-index microparticles with a quasi-perfect optical vortex. *Appl Opt* **57**, 79–84 (2018).
116. Hadad B, Froim S, Nagar H, Admon T, Eliezer Y et al. Particle trapping and conveying using an optical Archimedes' screw. *Optica* **5**, 551–556 (2018).
117. Wen JS, Gao BJ, Zhu GY, Liu DD, Wang LG. Precise position and angular control of optical trapping and manipulation via a single vortex-pair beam. *Opt Lasers Eng* **148**, 106773 (2022).
118. Sainis SK, Germain V, Mejean CO, Dufresne ER. Electrostatic interactions of colloidal particles in nonpolar solvents: role of surface chemistry and charge control agents. *Langmuir* **24**, 1160–1164 (2008).
119. Di Leonardo R, Keen S, Leach J, Saunter CD, Love GD et al. Eigenmodes of a hydrodynamically coupled micron-size multiple-particle ring. *Phys Rev E* **76**, 061402 (2007).
120. Di Leonardo R, Saglimbeni F, Ruocco G. Very-long-range nature of capillary interactions in liquid films. *Phys Rev Lett* **100**, 106103 (2008).
121. van der Horst A, Forde NR. Calibration of dynamic holographic optical tweezers for force measurements on biomaterials. *Opt Express* **16**, 20987–21003 (2008).
122. Mejean CO, Schaefer AW, Millman EA, Forscher P, Dufresne ER. Multiplexed force measurements on live cells with holographic optical tweezers. *Opt Express* **17**, 6209–6217 (2009).
123. Di Leonardo R, Leach J, Mushfique H, Cooper JM, Ruocco G et al. Multipoint holographic optical velocimetry in microfluidic systems. *Phys Rev Lett* **96**, 134502 (2006).
124. Mushfique H, Leach J, Di Leonardo R, Padgett MJ, Cooper JM. Optically driven pumps and flow sensors for microfluidic systems. *Proc Inst Mech Eng Part C J Mech Eng Sci* **222**, 829–837 (2008).
125. Woerdemann M, Alpmann C, Hörner F, Devaux A, De Cola L et al. Optical control and dynamic patterning of zeolites. *Proc SPIE* **7762**, 77622E (2010).
126. Ghadiri R, Surbek M, Esen C, Ostendorf A. Optically based manufacturing with polymer particles. *Phys Procedia* **5**, 47–51 (2010).
127. Cojoc D, Emiliani V, Ferrari E, Malureanu R, Cabrini S et al. Multiple optical trapping by means of diffractive optical elements. *Jpn J Appl Phys* **43**, 3910–3915 (2004).
128. Jesacher A, Fürhapter S, Bernet S, Ritsch-Marte M. Size selective trapping with optical "cogwheel" tweezers. *Opt Express* **12**, 4129–4135 (2004).
129. Hermerschmidt A, Krüger S, Haist T, Zwick S, Warber M et al.

Holographic optical tweezers with real-time hologram calculation using a phase-only modulating LCOS-based SLM at 1064 nm. *Proc SPIE* **6905**, 690508 (2008).
130. Zwick S, Haist T, Miyamoto Y, He L, Warber M et al. Holographic twin traps. *J Opt A Pure Appl Opt* **11**, 034011 (2009).
131. Jesacher A, Maurer C, Fürhapter S, Schwaighofer A, Bernet S et al. Optical tweezers of programmable shape with transverse scattering forces. *Opt Commun* **281**, 2207–2212 (2008).
132. Kim H, Lee W, Lee HG, Jo H, Song Y et al. *In situ* single-atom array synthesis using dynamic holographic optical tweezers. *Nat Commun* **7**, 13317 (2016).
133. Montes-Usategui M, Pleguezuelos E, Andilla J, Martín-Badosa E. Fast generation of holographic optical tweezers by random mask encoding of Fourier components. *Opt Express* **14**, 2101–2107 (2006).
134. Lizana A, Zhang HL, Turpin A, Van Eeckhout A, Torres-Ruiz FA et al. Generation of reconfigurable optical traps for microparticles spatial manipulation through dynamic split lens inspired light structures. *Sci Rep* **8**, 11263 (2018).
135. Schonbrun E, Piestun R, Jordan P, Cooper J, Wulff KD et al. 3D interferometric optical tweezers using a single spatial light modulator. *Opt Express* **13**, 3777–3786 (2005).
136. Köhler J, Ruschke J, Ferenz KB, Esen C, Kirsch M et al. Investigation of albumin-derived perfluorocarbon-based capsules by holographic optical trapping. *Biomed Opt Express* **9**, 743–754 (2018).
137. Suarez RAB, Ambrosio LA, Neves AAR, Zamboni-Rached M, Gesualdi MRR. Experimental optical trapping with frozen waves. *Opt Lett* **45**, 2514–2517 (2020).
138. Lamperska W, Drobczyński S, Nawrot M, Wasylczyk P, Masajada J. Micro-dumbbells—A versatile tool for optical tweezers. *Micromachines* **9**, 277 (2018).
139. Ashkin A, Dziedzic JM, Bjorkholm JE, Chu S. Observation of a single-beam gradient force optical trap for dielectric particles. *Opt Lett* **11**, 288–290 (1986).
140. Jesacher A, Fürhapter S, Bernet S, Ritsch-Marte M. Diffractive optical tweezers in the Fresnel regime. *Opt Express* **12**, 2243–2250 (2004).
141. López-Quesada C, Andilla J, Martín-Badosa E. Correction of aberration in holographic optical tweezers using a Shack-Hartmann sensor. *Appl Opt* **48**, 1084–1090 (2009).
142. Farré A, Shayegan M, López-Quesada C, Blab GA, Montes-Usategui M et al. Positional stability of holographic optical traps. *Opt Express* **19**, 21370–21384 (2011).
143. Martinez JL, Fernandez EJ, Prieto PM, Artal P. Chromatic aberration control with liquid crystal spatial phase modulators. *Opt Express* **25**, 9793–9801 (2017).
144. Chen J, Kong LJ, Zhan QW. Demonstration of a vectorial optical field generator with adaptive close loop control. *Rev Sci Instrum* **88**, 125111 (2017).
145. Wang LW, Yan W, Li RZ, Weng XY, Zhang J et al. Aberration correction for improving the image quality in STED microscopy using the genetic algorithm. *Nanophotonics* **7**, 1971–1980 (2018).
146. Chandra AD, Banerjee A. Rapid phase calibration of a spatial light modulator using novel phase masks and optimization of its efficiency using an iterative algorithm. *J Mod Opt* **67**, 628–637 (2020).
147. Khorin PA, Porfirev AP, Khonina SN. Adaptive detection of wave aberrations based on the multichannel filter. *Photonics* **9**, 204 (2022).
148. Zeylikovich I, Sztul HI, Kartazaev V, Le T, Alfano RR. Ultrashort Laguerre-Gaussian pulses with angular and group velocity dispersion compensation. *Opt Letters* **32**, 2025–2027 (2007).
149. Hahn J, Kim H, Choi K, Lee B. Real-time digital holographic beam-shaping system with a genetic feedback tuning loop. *Appl Opt* **45**, 915–924 (2006).
150. Frumker E, Silberberg Y. Femtosecond pulse shaping using a two-dimensional liquid-crystal spatial light modulator. *Opt Lett* **32**, 1384–1386 (2007).
151. Li RJ, Gao YH, Cao LC. *In situ* calibration for a phase-only spatial light modulator based on digital holography. *Opt Eng* **59**, 053101 (2020).
152. Jesacher A, Schwaighofer A, Fürhapter S, Maurer C, Bernet S et al. Wavefront correction of spatial light modulators using an optical vortex image. *Opt Express* **15**, 5801–5808 (2007).
153. Jiang Wenhan. Overview of adaptive optics development. *Opto-Electronic Eng* **45**, 170489 (2018).
154. Mu QQ, Cao ZL, Hu LF, Li DY, Xuan L. Adaptive optics imaging system based on a high-resolution liquid crystal on silicon device. *Opt Express* **14**, 8013–8018 (2006).
155. Mu QQ, Cao ZL, Li DY, Hu LF, Xuan L. Liquid crystal based adaptive optics system to compensate both low and high order aberrations in a model eye. *Opt Express* **15**, 1946–1953 (2007).
156. Liu TL, Upadhyayula S, Milkie DE, Singh V, Wang K et al. Observing the cell in its native state: Imaging subcellular dynamics in multicellular organisms. *Science* **360**, eaaq1392 (2018).
157. Ji N, Milkie DE, Betzig E. Adaptive optics via pupil segmentation for high-resolution imaging in biological tissues. *Nat Methods* **7**, 141–147 (2010).
158. Xavier J, Dasgupta R, Ahlawat S, Joseph J, Gupta PK. Three dimensional optical twisters-driven helically stacked multilayered microrotors. *Appl Phys Lett* **100**, 121101 (2012).
159. Yan W, Yang YL, Tan Y, Chen X, Li Y et al. Coherent optical adaptive technique improves the spatial resolution of STED microscopy in thick samples. *Photonics Res* **5**, 176–181 (2017).
160. Fürhapter S, Jesacher A, Bernet S, Ritsch-Marte M. Spiral interferometry. *Opt Lett* **30**, 1953–1955 (2005).
161. Zhao SA, Chung PS. Digital speckle shearing interferometer using a liquid-crystal spatial light modulator. *Opt Eng* **45**, 105606 (2006).
162. Maurer C, Bernet S, Ritsch-Marte M. Refining common path interferometry with a spiral phase Fourier filter. *J Opt A Pure Appl Opt* **11**, 094023 (2009).
163. Jesacher A, Fürhapter S, Bernet S, Ritsch-Marte M. Spiral interferogram analysis. *J Opt Soc Am A* **23**, 1400–1409 (2006).
164. Hai N, Rosen J. Single-plane and multiplane quantitative phase imaging by self-reference on-axis holography with a phase-shifting method. *Opt Express* **29**, 24210–24225 (2021).
165. Leach J, Keen S, Padgett MJ, Saunter C, Love GD. Direct measurement of the skew angle of the Poynting vector in a helically phased beam. *Opt Express* **14**, 11919–11924 (2006).
166. Mateo MP, Garcia CC, Hergenröder R. Depth analysis of polymer-coated steel samples using near-infrared femtosecond laser ablation inductively coupled plasma mass spectrometry. *Anal Chem* **79**, 4908–4914 (2007).
167. Xue S, Chen SY, Fan ZB, Zhai DD. Adaptive wavefront interferometry for unknown free-form surfaces. *Opt Express* **26**,

21910–21928 (2018).
168. van Putten EG, Lagendijk A, Mosk AP. Nonimaging speckle interferometry for high-speed nanometer-scale position detection. *Opt Letters* **37**, 1070–1072 (2012).
169. Dorrah AH, Zamboni-Rached M, Mojahedi M. Experimental demonstration of tunable refractometer based on orbital angular momentum of longitudinally structured light. *Light Sci Appl* **7**, 40 (2018).
170. Büttner L, Thümmler M, Czarske J. Velocity measurements with structured light transmitted through a multimode optical fiber using digital optical phase conjugation. *Opt Express* **28**, 8064–8075 (2020).
171. Huang GQ, Wu DX, Luo JW, Huang Y, Shen YC. Retrieving the optical transmission matrix of a multimode fiber using the extended Kalman filter. *Opt Express* **28**, 9487–9500 (2020).
172. Vijayakumar A, Rosen J. Interferenceless coded aperture correlation holography–a new technique for recording incoherent digital holograms without two-wave interference. *Opt Express* **25**, 13883–13896 (2017).
173. Vijayakumar A, Rosen J. Spectrum and space resolved 4D imaging by coded aperture correlation holography (COACH) with diffractive objective lens. *Opt Lett* **42**, 947–950 (2017).
174. Dubey N, Rosen J, Gannot I. High-resolution imaging system with an annular aperture of coded phase masks for endoscopic applications. *Opt Express* **28**, 15122–15137 (2020).
175. Vellekoop IM, Mosk AP. Focusing coherent light through opaque strongly scattering media. *Opt Lett* **32**, 2309–2311 (2007).
176. Van Beijnum F, Van Putten EG, Lagendijk A, Mosk AP. Frequency bandwidth of light focused through turbid media. *Opt Lett* **36**, 373–375 (2011).
177. Kashter Y, Vijayakumar A, Rosen J. Resolving images by blurring: superresolution method with a scattering mask between the observed objects and the hologram recorder. *Optica* **4**, 932–939 (2017).
178. Chen L, Chen ZY, Singh RK, Pu JX. Imaging of polarimetric-phase object through scattering medium by phase shifting. *Opt Express* **28**, 8145–8155 (2020).
179. Singh D, Singh RK. Lensless Stokes holography with the Hanbury Brown-Twiss approach. *Opt Express* **26**, 10801–10812 (2018).
180. Funamizu H, Uozumi J. Generation of fractal speckles by means of a spatial light modulator. *Opt Express* **15**, 7415–7422 (2007).
181. Carbonell-Leal M, Mínguez-Vega G, Lancis J, Mendoza-Yero M. Encoding of arbitrary micrometric complex illumination patterns with reduced speckle. *Opt Express* **27**, 19788–19801 (2019).
182. Cui M, Yang CH. Implementation of a digital optical phase conjugation system and its application to study the robustness of turbidity suppression by phase conjugation. *Opt Express* **18**, 3444–3455 (2010).
183. Fan WR, Hu XS, Zhaxi BM, Chen ZY, Pu JX. Generation of focal pattern with controllable polarization and intensity for laser beam passing through a multi-mode fiber. *Opt Express* **26**, 7693–7700 (2018).
184. Li DY, Sahoo SK, Lam HQ, Wang D, Dang C. Non-invasive optical focusing inside strongly scattering media with linear fluorescence. *Appl Phys Lett* **116**, 241104 (2020).
185. Zhang K, Wang ZY, Zhao HH, Liu C, Zhang HY et al. Implementation of an off-axis digital optical phase conjugation system for turbidity suppression on scattering medium. *Appl Sci* **10**, 875 (2020).
186. Cheng ZT, Wang LV. Focusing light into scattering media with ultrasound-induced field perturbation. *Light Sci Appl* **10**, 159 (2021).
187. Wu P, Zhang DJ, Yuan J, Zeng SQ, Gong H et al. Large depth-of-field fluorescence microscopy based on deep learning supported by Fresnel incoherent correlation holography. *Opt Express* **30**, 5177–5191 (2022).
188. Chen HK, Wu XJ, Zhang YQ, Yang Y, Min CJ et al. Wide-field *in situ* multiplexed Raman imaging with superresolution. *Photonics Res* **6**, 530–534 (2018).
189. Paterson L, Agate B, Comrie M, Ferguson R, Lake TK et al. Photoporation and cell transfection using a violet diode laser. *Opt Express* **13**, 595–600 (2005).
190. Ng JW, Chatenay D, Robert J, Poirier MG. Plasmid copy number noise in monoclonal populations of bacteria. *Phys Rev E* **81**, 011909 (2010).
191. Wang P, Slipchenko MN, Mitchell J, Yang C, Potma EO et al. Far-field imaging of non-fluorescent species with subdiffraction resolution. *Nat Photonics* **7**, 449–453 (2013).
192. Reda F, Salvatore M, Borbone F, Maddalena P, Ambrosio A et al. Varifocal diffractive lenses for multi-depth microscope imaging. *Opt Express* **30**, 12695–12711 (2022).
193. Buckley C, Carvalho MT, Young LK, Rider SA, McFadden C et al. Precise spatio-temporal control of rapid optogenetic cell ablation with mem-KillerRed in Zebrafish. *Sci Rep* **7**, 5096 (2017).
194. Rodrigo JA, Soto JM, Alieva T. Fast label-free microscopy technique for 3D dynamic quantitative imaging of living cells. *Biomed Opt Express* **8**, 5507–5517 (2017).
195. Wang ZJ, Cai YA, Liang YS, Zhou X, Yan SH et al. Single shot, three-dimensional fluorescence microscopy with a spatially rotating point spread function. *Biomed Opt Express* **8**, 5493–5506 (2017).
196. Leach J, Yao E, Padgett MJ. Observation of the vortex structure of a non-integer vortex beam. *New J Phys* **6**, 71 (2004).
197. Leach J, Dennis MR, Courtial J, Padgett MJ. Knotted threads of darkness. *Nature* **432**, 165 (2004).
198. Leach J, Dennis MR, Courtial J, Padgett MJ. Vortex knots in light. *New J Phys* **7**, 55 (2005).
199. Tao SH, Yuan XC, Lin J, Peng X, Niu HB. Fractional optical vortex beam induced rotation of particles. *Opt Express* **13**, 7726–7731 (2005).
200. Hu JT, Tai YP, Zhu LH, Long ZX, Tang MM et al. Optical vortex with multi-fractional orders. *Appl Phys Lett* **116**, 201107 (2020).
201. Hu XB, Perez-Garcia B, Rodríguez-Fajardo V, Hernandez-Aranda RI, Forbes A et al. Free-space local nonseparability dynamics of vector modes. *Photonics Res* **9**, 439–445 (2021).
202. Shen YJ, Nape I, Yang XL, Fu X, Gong ML et al. Creation and control of high-dimensional multi-partite classically entangled light. *Light Sci Appl* **10**, 50 (2021).
203. Malik M, Mirhosseini M, Lavery MPJ, Leach J, Padgett MJ et al. Direct measurement of a 27-dimensional orbital-angular-momentum state vector. *Nat Commun* **5**, 3115 (2014).
204. Zhang J, Huang SJ, Zhu FQ, Shao W, Chen MS. Dimensional properties of Laguerre–Gaussian vortex beams. *Appl Opt* **56**, 3556–3561 (2017).

205. Shao ZK, Zhu JB, Chen YJ, Zhang YF, Yu SY. Spin-orbit interaction of light induced by transverse spin angular momentum engineering. *Nat Commun* **9**, 926 (2018).
206. Pan SZ, Pei CY, Liu S, Wei J, Wu D et al. Measuring orbital angular momentums of light based on petal interference patterns. *OSA Continuum* **1**, 451–461 (2018).
207. Li XZ, Zhang H. Anomalous ring-connected optical vortex array. *Opt Express* **28**, 13775–13785 (2020).
208. Lu JN, Cao CY, Zhu ZQ, Gu B. Flexible measurement of high-order optical orbital angular momentum with a variable cylindrical lens pair. *Appl Phys Lett* **116**, 201105 (2020).
209. Klug A, Peters C, Forbes A. Robust structured light in atmospheric turbulence. *Adv Photonics* **5**, 016006–016006 (2023).
210. Emile O, Emile J, Brousseau C. Rotational Doppler shift upon reflection from a right angle prism. *Appl Phys Lett* **116**, 221102 (2020).
211. Li DH, Bongiovanni D, Goutsoulas M, Xia SQ, Zhang Z et al. Direct comparison of anti-diffracting optical pin beams and abruptly autofocusing beams. *OSA Continuum* **3**, 1525–1535 (2020).
212. Xu YQ, Li X, Zhou L, Zhou YM, Wang F et al. Experimental investigation in Airy transform of Gaussian beams with optical vortex. *Results Phys* **28**, 104588 (2021).
213. Fu SY, Hai L, Song R, Gao CQ, Zhang XD. Representation of total angular momentum states of beams through a four-parameter notation. *New J Phys* **23**, 083015 (2021).
214. Kesarwani R, Simbulan KB, Huang TD, Chiang YF, Yeh NC et al. Control of trion-to-exciton conversion in monolayer WS_2 by orbital angular momentum of light. *Sci Adv* **8**, eabm0100 (2022).
215. Li XZ, Ma HX, Yin CL, Tang J, Li HH et al. Controllable mode transformation in perfect optical vortices. *Opt Express* **26**, 651–662 (2018).
216. Li L, Chang CL, Yuan XZ, Yuan CJ, Feng ST et al. Generation of optical vortex array along arbitrary curvilinear arrangement. *Opt Express* **26**, 9798–9812 (2018).
217. Szatkowski M, Masajada J, Augustyniak I, Nowacka K. Generation of composite vortex beams by independent Spatial Light Modulator pixel addressing. *Opt Commun* **463**, 125341 (2020).
218. Kumar P, Pal SK, Nishchal NK, Senthilkumaran P. Non-interferometric technique to realize vector beams embedded with polarization singularities. *J Opt Soc Am A* **37**, 1043–1052 (2020).
219. Meng WJ, Hua YL, Cheng K, Li BL, Liu TT et al. 100 Hertz frame-rate switching three-dimensional orbital angular momentum multiplexing holography via cross convolution. *Opto-Electron Sci* **1**, 220004 (2022).
220. Lochab P, Senthilkumaran P, Khare K. Robust laser beam engineering using polarization and angular momentum diversity. *Opt Express* **25**, 17524–17529 (2017).
221. Wu Y, Ni R, Xu Z, Wu YD, Fang XY et al. Tunable third harmonic generation of vortex beams in an optical superlattice. *Opt Express* **25**, 30820–30826 (2017).
222. Li H, Liu HG, Chen XF. Nonlinear generation of Airy vortex beam. *Opt Express* **26**, 21204–21209 (2018).
223. Otte E, Tekce K, Lamping S, Ravoo BJ, Denz C. Polarization nano-tomography of tightly focused light landscapes by self-assembled monolayers. *Nat Commun* **10**, 4308 (2019).
224. Bernet S, Jesacher A, Fürhapter S, Maurer C, Ritsch-Marte M. Quantitative imaging of complex samples by spiral phase contrast microscopy. *Opt Express* **14**, 3792–3805 (2006).
225. Situ GH, Pedrini G, Osten W. Spiral phase filtering and orientation-selective edge detection/enhancement. *J Opt Soc Am A* **26**, 1788–1797 (2009).
226. Tao SH, Yuan XC, Lin J, Burge RE. Residue orbital angular momentum in interferenced double vortex beams with unequal topological charges. *Opt Express* **14**, 535–541 (2006).
227. Forbes A, Ramachandran S, Zhan QW. Photonic angular momentum: progress and perspectives. *Nanophotonics* **11**, 625–631 (2022).
228. Chen J, Chen X, Li T, Zhu SN. On - chip detection of orbital angular momentum beam by plasmonic nanogratings. *Laser Photonics Rev* **12**, 1700331 (2018).
229. Stütz M, Gröblacher S, Jennewein T, Zeilinger A. How to create and detect *N*-dimensional entangled photons with an active phase hologram. *Appl Phys Lett* **90**, 261114 (2007).
230. Zhu FQ, Huang SJ, Shao W, Zhang J, Chen MS et al. Free-space optical communication link using perfect vortex beams carrying orbital angular momentum (OAM). *Opt Commun* **396**, 50–57 (2017).
231. Shao W, Huang SJ, Liu XP, Chen MS. Free-space optical communication with perfect optical vortex beams multiplexing. *Opt Commun* **427**, 545–550 (2018).
232. Malik M, O'Sullivan M, Rodenburg B, Mirhosseini M, Leach J et al. Influence of atmospheric turbulence on optical communications using orbital angular momentum for encoding. *Opt Express* **20**, 13195–13200 (2012).
233. Wang LX, Nejad RM, Corsi A, Lin JC, Messaddeq Y et al. Linearly polarized vector modes: enabling MIMO-free mode-division multiplexing. *Opt Express* **25**, 11736–11749 (2017).
234. Jing GQ, Chen LZ, Wang PP, Xiong WJ, Huang ZB et al. Recognizing fractional orbital angular momentum using feed forward neural network. *Results Phys* **28**, 104619 (2021).
235. Trichili A, Rosales-Guzmán C, Dudley A, Ndagano B, Ben Salem A et al. Optical communication beyond orbital angular momentum. *Sci Rep* **6**, 27674 (2016).
236. Erhard M, Fickler R, Krenn M, Zeilinger A. Twisted photons: new quantum perspectives in high dimensions. *Light Sci Appl* **7**, 17146 (2018).
237. Forbes A, Nape I. Quantum mechanics with patterns of light: progress in high dimensional and multidimensional entanglement with structured light. *AVS Quantum Sci* **1**, 011701 (2019).
238. Mair A, Vaziri A, Weihs G, Zeilinger A. Entanglement of the orbital angular momentum states of photons. *Nature* **412**, 313–316 (2001).
239. Jack B, Leach J, Ritsch H, Barnett M, Padgett MJ et al. Precise quantum tomography of photon pairs with entangled orbital angular momentum. *New J Phys* **11**, 103024 (2009).
240. Agnew M, Leach J, McLaren M, Stef Roux F, Boyd RW. Tomography of the quantum state of photons entangled in high dimensions. *Phys Rev A* **84**, 062101 (2011).
241. Dada AC, Leach J, Buller GS, Padgett MJ, Andersson E. Experimental high-dimensional two-photon entanglement and violations of generalized Bell inequalities. *Nat Phys* **7**, 677–680 (2011).
242. Leach J, Jack B, Romero J, jha AK, Yao AM et al. Quantum correlations in optical angle–orbital angular momentum variables. *Science* **329**, 662–665 (2010).
243. Nape I, Rodríguez-Fajardo V, Zhu F, Huang HC, Leach J et al. Measuring dimensionality and purity of high-dimensional en-

tangled states. *Nat Commun* **12**, 5159 (2021).
244. Bavaresco J, Herrera Valencia N, Klöckl C, Pivoluska M, Erker P et al. Measurements in two bases are sufficient for certifying high-dimensional entanglement. *Nat Phys* **14**, 1032–1037 (2018).
245. Kovlakov EV, Straupe SS, Kulik SP. Quantum state engineering with twisted photons via adaptive shaping of the pump beam. *Phys Rev A* **98**, 060301(R) (2018).
246. Walborn SP, de Oliveira AN, Pádua S, Monken CH. Multimode hong-ou-mandel interference. *Phys Rev Lett* **90**, 143601 (2003).
247. Bornman N, Tavares Buono W, Lovemore M, Forbes A. Optimal pump shaping for entanglement control in any countable basis. *Adv Quantum Technol* **4**, 2100066 (2021).
248. McLaren M, Mhlanga T, Padgett MJ, Roux FS, Forbes A. Self-healing of quantum entanglement after an obstruction. *Nat Commun* **5**, 3248 (2014).
249. Zhang YW, Roux FS, Konrad T, Agnew M, Leach J et al. Engineering two-photon high-dimensional states through quantum interference. *Sci Adv* **2**, e1501165 (2016).
250. De Oliveira M, Bornman N, Forbes A. Holographically controlled random numbers from entangled twisted photons. *Phys Rev A* **102**, 032620 (2020).
251. Mafu M, Dudley A, Goyal S, Giovannini D, McLaren M et al. Higher-dimensional orbital-angular-momentum-based quantum key distribution with mutually unbiased bases. *Phys Rev A* **88**, 032305 (2013).
252. Mirhosseini M, Magaña-Loaiza OS, O'Sullivan MN, Rodenburg B, Malik M et al. High-dimensional quantum cryptography with twisted light. *New J Phys* **17**, 033033 (2015).
253. Sit A, Bouchard F, Fickler R, Gagnon-Bischoff J, Larocque H et al. High-dimensional intracity quantum cryptography with structured photons. *Optica* **4**, 1006–1010 (2017).
254. Cozzolino D, Bacco D, Da Lio B, Ingerslev K, Ding YH et al. Orbital angular momentum states enabling fiber-based high-dimensional quantum communication. *Phys Rev Appl* **11**, 064058 (2019).
255. Pinnell J, Nape I, de Oliveira M, TabeBordbar N, Forbes A. Experimental demonstration of 11-dimensional 10-party quantum secret sharing. *Laser Photonics Rev* **14**, 2000012 (2020).
256. Zhang YW, Agnew M, Roger T, Roux FS, Konrad T et al. Simultaneous entanglement swapping of multiple orbital angular momentum states of light. *Nat Commun* **8**, 632 (2017).
257. Sephton B, Vallés A, Nape I, Cox MA, Steinlechner F et al. Stimulated teleportation of high-dimensional information with a nonlinear spatial mode detector. arXiv: 2111.13624 (2021).
258. Krenn M, Huber M, Fickler R, Lapkiewicz R, Ramelow S et al. Generation and confirmation of a (100× 100)-dimensional entangled quantum system. *Proc Natl Acad Sci USA* **111**, 6243–6247 (2014).
259. Shapiro JH, Boyd RW. The physics of ghost imaging. *Quantum Inf Process* **11**, 949–993 (2012).
260. Padgett MJ, Boyd RW. An introduction to ghost imaging: quantum and classical. *Philos Trans Roy Soc A Math Phys Eng Sci* **375**, 20160233 (2017).
261. Gatti A, Brambilla E, Lugiato L. Quantum imaging. *Prog Opt* **51**, 251–348 (2008).
262. Edgar MP, Gibson GM, Padgett MJ. Principles and prospects for single-pixel imaging. *Nat Photonics* **13**, 13–20 (2019).
263. Mansha S, Moitra P, Xu XW, Mass TWW, Veetil RM et al. High resolution multispectral spatial light modulators based on tunable Fabry-Perot nanocavities. *Light Sci Appl* **11**, 141 (2022).

Acknowledgements

We are grateful for financial supports from National Natural Science Foundation of China (No. 62235009).

Author contributions

Each author contributed significantly to the review. YQ Yang was primarily responsible for developing the initial idea and drafting the original manuscript. A Forbes collected the data and contributed to both the review and editing of the manuscript. LC Cao provided necessary resources and supervised the project. All authors have read and approved the final version of the manuscript for submission and publication.

Competing interests

The authors declare no competing financial interests.